SANDIA REPORT

SAND2011-8421
Unlimited Release
Printed September 2011

Experimental Characterization of Energetic Material Dynamics for Multiphase Blast Simulation

Steven J. Beresh, Sean P. Kearney, Justin L. Wagner, Brian O. M. Pruett, Elton K. Wright, and Melvin R. Baer

Prepared by
Sandia National Laboratories
Albuquerque, New Mexico 87185 and Livermore, California 94550

Sandia National Laboratories is a multi-program laboratory managed and operated by Sandia Corporation, a wholly owned subsidiary of Lockheed Martin Corporation, for the U.S. Department of Energy's National Nuclear Security Administration under contract DE-AC04-94AL85000.

Issued by Sandia National Laboratories, operated for the United States Department of Energy by Sandia Corporation.

Available to DOE and DOE contractors from
U.S. Department of Energy
Office of Scientific and Technical Information
P.O. Box 62
Oak Ridge, TN 37831

Telephone: (865)576-8401
Facsimile: (865)576-5728
E-Mail: reports@adonis.osti.gov
Online ordering: http://www.osti.gov/bridge

Available to the public from
U.S. Department of Commerce
National Technical Information Service
5285 Port Royal Rd
Springfield, VA 22161

Telephone: (800)553-6847
Facsimile: (703)605-6900
E-Mail: orders@ntis.fedworld.gov
Online order: http://www.ntis.gov/help/ordermethods.asp?loc=7-4-0#online

SAND2011-8421
Unlimited Release
Printed September 2011

Experimental Characterization of Energetic Material Dynamics for Multiphase Blast Simulation

Steven J. Beresh, Sean P. Kearney, Justin L. Wagner, Brian O. M. Pruett, Elton K. Wright, and Melvin R. Baer
Sandia National Laboratories
PO Box 5800
Albuquerque, New Mexico 87185-0825

Abstract

Currently there is a substantial lack of data for interactions of shock waves with particle fields having volume fractions residing between the dilute and granular regimes, which creates one of the largest sources of uncertainty in the simulation of energetic material detonation. To close this gap, a novel Multiphase Shock Tube has been constructed to drive a planar shock wave into a dense gas-solid field of particles. A nearly spatially isotropic field of particles is generated in the test section by a gravity-fed method that results in a spanwise curtain of spherical 100-micron particles having a volume fraction of about 19%. Interactions with incident shock Mach numbers of 1.66, 1.92, and 2.02 were achieved. High-speed schlieren imaging simultaneous with high-frequency wall pressure measurements are used to reveal the complex wave structure associated with the interaction. Following incident shock impingement, transmitted and reflected shocks are observed, which lead to differences in particle drag across the streamwise dimension of the curtain. Shortly thereafter, the particle field begins to propagate downstream and spread. For all three Mach numbers tested, the energy and momentum fluxes in the induced flow far downstream are reduced about 30-40% by the presence of the particle field. X-Ray diagnostics have been developed to penetrate the opacity of the flow, revealing the concentrations throughout the particle field as it expands and spreads downstream with time. Furthermore, an X-Ray particle tracking velocimetry diagnostic has been demonstrated to be feasible for this flow, which can be used to follow the trajectory of tracer particles seeded into the curtain. Additional experiments on single spherical particles accelerated behind an incident shock

wave have shown that elevated particle drag coefficients can be attributed to increased compressibility rather than flow unsteadiness, clarifying confusing results from the historical database of shock tube experiments. The development of the Multiphase Shock Tube and associated diagnostic capabilities offers experimental capability to a previously inaccessible regime, which can provide unprecedented data concerning particle dynamics of dense gas-solid flows.

CONTENTS

FIGURES

TABLES

1. Introduction

1.1. Motivation

Accurate simulation of energetic material detonation is crucial to a variety of national interests involving explosive devices, including vulnerability of weapons and structures to nearby explosions, blast mitigation, IED protection, and enhanced blasts. Unfortunately, such predictive capability is limited by a lack of knowledge of the underlying phenomena of the earliest stages of the blast, where the particle dynamics of the fragmented materials within the gas expansion products are pivotal to understanding the continuing reaction. The complication is that, at the explosion's onset, the particles are densely packed within the expanding flow, whereas our knowledge of the process is restricted to dilute concentrations. We propose to fill this gap by constructing an unprecedented multiphase shock tube that can drive a shock front into a particle/gas mixture of a selected volume fraction, then measure the motion of the densely-packed particles within the expanding gas. One of the great challenges of the problem is that the opacity of the flow prevents usage of common fluid dynamics diagnostics and instead will require the development of unconventional measurement approaches. We seek to exploit measurement concepts previously utilized for multiphase flows and structural mechanics and adapt them to the uncommon difficulties of the present problem, particularly x-ray particle image velocimetry or a tomographic system using x-rays. Finally, while velocity measurements are of the greatest value, the lack of knowledge of this flowfield is so profound that even delivery of simpler measurements such as shock speeds and pressure histories would represent a valuable contribution. By providing crucial new physical data, we can boost the level of fidelity in algorithms used to simulate blasts in national security applications.

The difficulty of experimentally addressing this problem is multifaceted. First, a facility must be built that is capable of representing, in a safe and controlled manner, the flow physics found in the early moments of a detonation. One component of the project, therefore, will be devoted to the design, construction, and testing of the proposed two-phase shock tube, which itself would be without peer. Differing from a traditional shock tube, the driven section will incorporate a means to suspend a concentration of particles representative of energetic materials as they fragment immediately following detonation. When the shock tube is fired, a shock front will be propelled into this dense mixture of driven gas and solid particles, entraining the particles in the wake of the accelerated gas in a fashion analogous to a sector of a three-dimensional blast. Fast response pressure instrumentation incorporated into the shock tube will track the propagation of the shock wave through the simulated reaction products and the associated pressure history. High-speed imaging can provide trajectory data for the particle field as the shock-induced fluid sweeps it downstream. The lack of knowledge for this flowfield is so profound that even delivery of relatively simple measurements such as these would represent a valuable contribution to improving blast simulation capability.

In concert with evolving the two-phase shock tube, we must develop measurement techniques that demonstrate potential to overcome the opacity of the flowfield and the short duration of events. The most promising approach appears to be particle image velocimetry (PIV) in the x-ray regime, since this radiation can penetrate the optically thick flowfield. X-ray velocimetry might also be achieved by time-based detection at two locations displaced in the streamwise direction, then correlating between the two signals created by the random passage of particle absorbers. The velocimetry techniques necessary for this flowfield are not simply new implementations of routine diagnostics and will require substantial development effort to create fresh technologies. To enable this process, we will build a simple benchtop flow facility that can replicate the opaque gas-solid mixture at low speeds and low pressures and with long operational times. Although such a flow is not representative of the fluid dynamics found in detonations, it does replicate many of the diagnostic challenges that must be overcome. We can develop several instrumentation approaches without the

difficulties associated with the two-phase shock tube, assess which are most likely to be useful, and only after we have solved the initial implementation will we begin to migrate it to its intended purpose.

Although explosives researchers have for many decades futilely sought gas dynamics data in densely packed shock-driven two-phase flows, more recent improvements in energetic materials and, most particularly, growth in nonintrusive measurement capabilities make this field currently ripe for further development. Even partial success would provide a unique capability within the broader national establishment and be of significant service to the explosives community.

1.2. Literature Review

Gas-solid flow can be categorized by its particle volume fraction φp of the flow. Zhang et al. [1] provide a good discussion of three particle volume fraction flow regimes and their physical significances. If the particle volume fraction is less than about 0.1%, the gas-solid flow is said to be in the "dilute," or "dusty" regime. In dilute two-phase flows, the volume fraction of particles is low enough such that the particle collisional effects are negligible. Therefore, the speed of sound and the pressure of the solid portion of the flow can be ignored [2]. In the dusty gas-solid flow regime, accepted expressions exist for the Nusselt number and the particle drag coefficient [3], which have been validated experimentally [4]. The expressions are used frequently in dilute gas flow simulations to model shock attenuation [5-7]. For gas-solid flows where the particles are randomly packed (φ_p greater than about 50%) the flow regime is said to be "granular." An example of such a flow would be the impingement of a normal shock on a pressed bed of explosive powders, such as in the experiments of Sheffield et al. [8], and Anderson et al. [9]. Simulations have shown promise in capturing the physics of shock-particle interactions in the granular regime. For example, applying the continuum mixture theory developed by Baer and Nunziato [10], Baer [11] was able to successfully model the normal shock impingement studies of Sheffield et al. [8], and Anderson et al. [9].

The previous discussion demonstrates that there exists a basic understanding of and ability to model shock-particle interactions in solid-gas flows that are either in the dilute particle volume fraction regime or the packed volume fraction regime. However, there is a substantial knowledge gap in studies addressing flow with intermediate particle volume fractions. Solid-gas flows in this regime have particle volume fractions between about 1 and 50%, and are known as "dense gas-solid flows" [1]. Dense gas-solid flows would exist at microsecond time scales during energetic material detonation where the shocked particles are closely spaced. Additionally, it is expected that the dense gas-solid flow will persist until the volume fraction of the accelerated particles has become sufficiently low within the expanding detonation products to be considered dilute. Dependable simulation of energetic material detonation requires an in depth understanding of the chemical reactions that occur during these early stages, but these simulations are significantly limited since there is a substantial lack of understanding of shock-particle interactions in dense solid-gas flows. Rogue et al. [12] provided a rare experiment in the dense gas-solid regime, where they measured the dispersion of stacked spheres in a vertical shock tube. Though they provided useful observations regarding the trajectory of the particle fronts and resulting pressure equilibration, much remains unknown regarding the shock-particle interactions that are involved in this flow regime. As a result of a lack of data, the effects of shock-particle interactions in current chemical kinetics models typically are extrapolated from data within the dilute and granular regimes, or are empirically based upon explosive field tests. Without data specifically acquired for dense gas-solid flows, the understanding of energetic material detonation and gas-solid flow during the early-time expansion, will continue to suffer from limited physical fidelity.

The novel diagnostics needed to cope with the opacity of the multiphase compressible flow are not entirely without precedent, although such techniques never been applied to a flow of the nature proposed herein. Seeger et al [13] developed an x-ray PIV system for chemical engineering

experiments in a bubble column, whereas Lee & Kim [14] used a somewhat different implementation of x-ray PIV for small low-speed flows and later applied it to a simulated blood flow. The only known high-speed flow in which x-ray particle tracking was employed is that of Xiao et al [15], but the particle concentration in this case was very low.

2. Baseline Shock Tube

2.1. Design and Operation

A schematic representation and photograph of the baseline shock tube without a particle seeding capability are shown in Fig. 1, and Fig. 2, respectively. The driver section is a 2.1 m long stainless steel pipe with an inner diameter of 88.9 mm and a wall thickness of 12.7 mm. A high-pressure compressed nitrogen system provides the driver gas. As discussed below, surge tanks having a total volume of 7.6 liters are used to limit the flow of nitrogen after a test begins. The pressurization of the driver pipe and surge tanks is controlled remotely with an in-house developed LabVIEW (National Instruments) code that instructs a Tescom (Model 26-2065-B24A352) dome-loaded pressure regulator system and two ASCO Redhat (Model 8262G200) solenoid valves. The driver gas pressure P_4 and the surge tank pressure are monitored with an Omega pressure transducer (Model PX01C1-1KG5T). A port on the driver end plate provides access for a thermocouple (T-type) to monitor the driver gas temperature T_4, which is typically near 300 K. Cruciform scored, nickel alloy burst disks (BS&B Safety Systems) are used as the diaphragms that initially separate the driver gas from the driven gas. The scoring of the burst disk ensures it opens in four petals preventing fragmentation. Burst disks with nominal burst pressures of 1100 kPa (160 psig), 2760 kPa (400 psig), and 4140 kPa (600 psig) have been used to produce shock Mach numbers of about 1.66, 1.95, and 2.05, respectively. According to the manufacturer, burst pressures are repeatable to 5%. The tube is designed to withstand a maximum driver pressure of about 4140 kPa (600 psig). As discussed below, the maximum P_4 is not based on the driver pipe itself, but on the resulting peak pressures expected in the driven sections. The last five driven sections have the thinnest walls and are thus the components that limit maximum allowable pressures. As seen in Fig. 1, the burst disk holder section follows the driver pipe. This section is circular with an inner diameter that matches the driver pipe and it has a length of 157.5 mm.

As shown in Fig. 1, the driven section consists of seven sections (D1-D7) made from extruded square aluminum tubing having a nominal wall thickness of 12.7 mm. The total driven length is 5.2 m. The driven sections are cut from one piece of extruded aluminum tubing having a nominal inner width of 76.2 mm. Since the inner width of the extruded square tubing was measured to vary by about 1 mm, the inner walls of the last five sections were all machined to a width of 79.2 ± 0.2 mm using an electrical discharge machine. A driven section with parallel planar walls was chosen to simplify the design and configuration of instrumentation such as pressure transducers and optical diagnostics systems. The modular design of the driven section allows for the simple insertion of a test section. Furthermore, the location of the test section is easily interchangeable. Typically, the driven gas is ambient air at an initial temperature of about 297 K and an initial atmospheric pressure of about 84.1 kPa. An Omega pressure transducer (Model PX01C1-1KG5T) and a thermocouple (T-type) are used to measure the driven initial conditions. Note that it is expected that the abrupt change from a circular diameter to a square inner hole will disrupt the initial shock. However, as is discussed below, the shock develops a very nearly planar front upon reaching the test section location.

A three-step process is used to pressurize the driver pipe and rupture the disk. Through the use of surge tanks that can be filled independently from the driver pipe, the process allows for the maximum possible pressure of the driver pipe to be precisely controlled as follows. First, both the surge tank and driver solenoid valves labeled in Fig. 1 are opened and the surge tanks and driver pipe are pressurized to a value about 6% below the rated disk burst pressure. Next the driver solenoid valve is closed and the pressure of the surge tanks is increased. At the shock Mach numbers of 1.66, 1.95, and 2.05, the surge tank is filled to 1970, 4220, and 5860 kPa, respectively. In the final step, the surge tank solenoid is closed and the driver solenoid is opened, which increases the driver pressure to a value

Transducer Locations

Transducer	x (m)
T1	0.9195
T2	1.5385
T3	2.6575
T4	3.3607
T5	3.7671
T6	4.1735
T7-T10*	4.5799
T11	4.9863
T12-T14**	5.1895

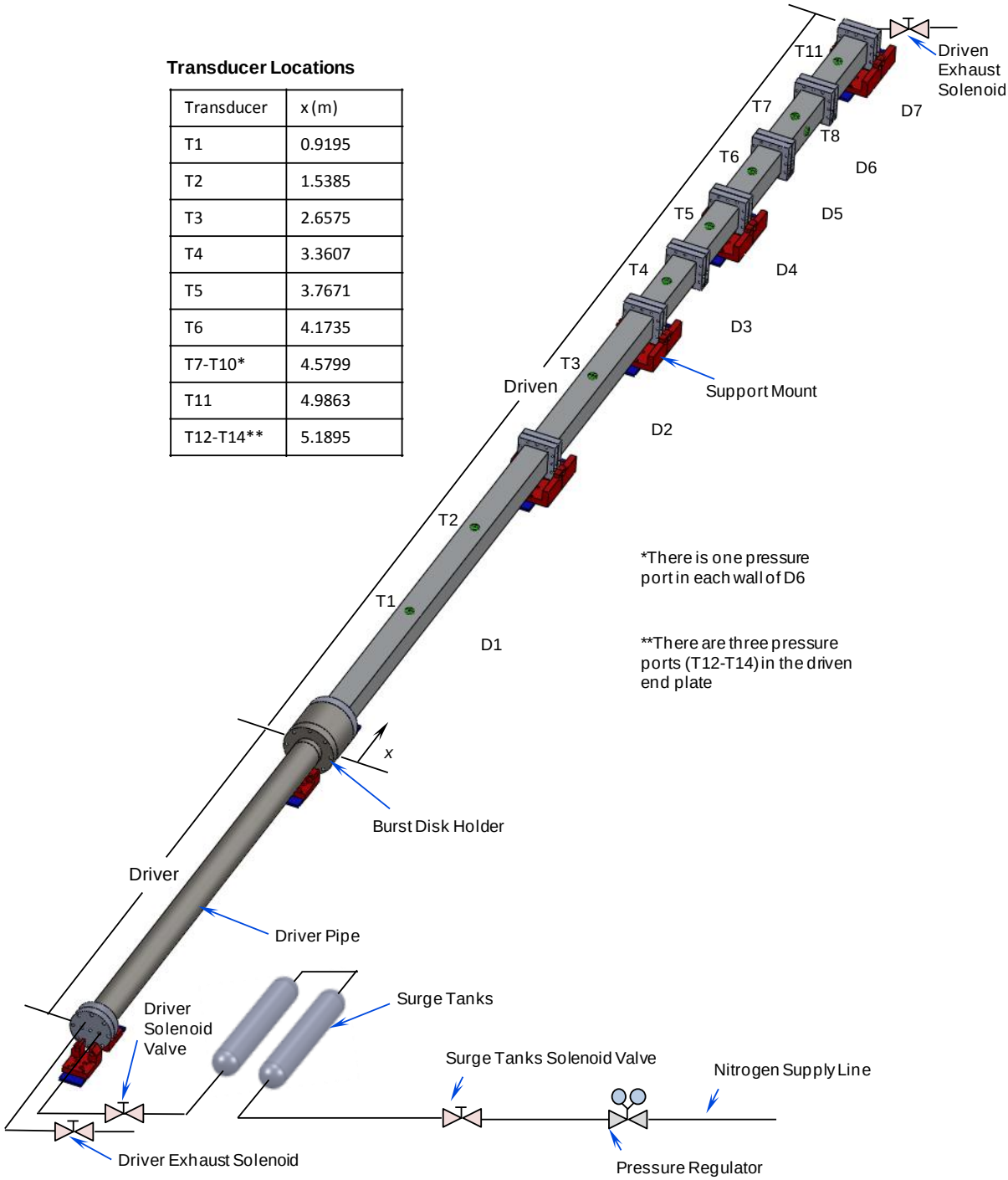

Fig. 1: Schematic of the baseline shock-tube including the location of high-frequency-response pressure transducers.

Fig. 2: Photograph of the baseline shock tube.

that bursts the disk. The system is designed so that it takes about 4 seconds for the driver pressure to increase from a value 6% lower than the rated burst pressure to a value 6% higher than rated pressure. This relatively long fill time is set with a needle valve and was chosen to maintain a close to quiescent driver section prior to the rupture of the disk.

As shown in Fig. 1, the tube is mounted to rail carriers (Newport CX95AS) with custom-made support mounts. The photograph in Fig. 2, shows the rail carriers that attach to a modular structural rail system (Newport X95) that supports the shock tube. The tube support system is designed such that after a test, the driver pipe unbolts from the holder section and is slid upstream allowing for the easy replacement of the burst disk. Once a test is completed, the tube can be exhausted through either a driver, or driven exhaust solenoid. Finally, although not shown in Fig. 1, the tube gas handling lines have multiple manual and pressure relief valves that prevent over-pressurization and accidental pressurization from occurring.

2.2. High-Frequency Pressure Measurements

Figure 1 shows the location of the high-frequency-response pressure transducers used to characterize the shock tube. A total of 14 flush-mounted pressure transducers are placed at port locations T1-T14. The transducer ports T1 through T6 are in the top wall along the length of the driven section. T1 provides a rising-edge trigger signal that begins the pressure data acquisition upon the arrival of the incident shock. In the sixth driven section (D6), there are four transducer locations in total (T7-T10), with one in each wall of the section, each at the same streamwise location. Four transducers are used in this section in order to determine the planarity of the initial shock. In addition, there are three transducer locations (T12-T14) in the end wall that also provide a measure of shock planarity. T12-T14 are placed at 120-degree separations along a 40.1 mm diameter circle with respect to the center of the end plate. For the 1100 kPa burst disk tests, the ports T1-T14 were instrumented

with PCB transducers (Model 113B27) having an output range of 0-1380 kPa. For the 2760 kPa burst disk tests, ports T1-T4 held PCB transducers (Model 113B27) and ports T5-T14 had PCB transducers (Model 113B26) with an output range of 0-6895 kPa. A signal conditioner box (PCB Model 483C) provides the transducers the constant current and the excitation voltage necessary for operation. The signal conditioner box also amplifies the sensor signals. The amplified signals are then low-pass filtered (Krohn-Hite Model 3384) with a cutoff frequency of 200 kHz. The filtered signals are sent to a data acquisition chassis (NI PXI 1505), in which two 14-bit data acquisition cards (NI PXI 6133) digitize the signals at a sampling frequency of 400 kHz. The digitized signals are then sent through fiber optic cables to a personal computer where they are recorded.

2.3. Characterization of the Baseline Shock Tube

Experimental test conditions acquired using the three nominal burst pressures are presented in Table 1. Using the pressure transducers to measure shock crossing times, the velocity of the shock W_s can be measured and the shock Mach number M_s can be calculated. Note that W_s in Table 1 corresponds to the velocity measured between T4 and T11. The experimental parameters presented in Table 1 are based on five tests each of the three burst disk nominal pressures. The ranges are 95% confidence bands are based on student-t theory.

Figure 3 shows *t-x* diagrams corresponding to two baseline shock tube tests. Figure 3a corresponds to a test with M_s = 1.66 and Fig. 3b corresponds to a test with M_s = 1.95. Shock crossing times measured with high-frequency pressure transducers are compared to the theoretical shock trajectories given by one-dimensional unsteady wave theory [16]. For both shock Mach numbers, it is evident that the shock velocity decays with increasing streamwise distance. At the test section centerline location of x = 4.58, the measured shock Mach numbers are about 0.1 lower than the theoretical values. Owing to pressure waves emanating from boundary layer growth [17], this attenuation is to be expected and it is consistent with that observed by other researchers using a shock tube having similar geometry and flow conditions [17]. In addition, evidence of the intersection of the contact surface with the reflected shock is observed in Fig. 3. For example, in Fig. 3a, the reflected shock deviates from a straight line trajectory between x = 4.17 and 3.76 m. Comparing the location of this deviation to that of the theoretical arrival of the contact surface therefore suggests that the contact surface and the reflected shock interact between about t = 12 and 14 ms. By the same argument, Fig. 3b suggests that the contact surface and reflected shock interact between about t = 9 and 11 ms. In tests involving shock-particle interactions, a test section of equivalent length replaces one of the last five driven sections. Note that for the standard use of a shock tube, the useful test time occurs after the passage of the incident shock and before either the arrival of the contact surface, or the arrival of the reflected shock [16]. The *t-x* diagrams of Fig. 3 and the previous discussion show that if the nominal M_s is 1.67, then the test section center line should be placed at x = 4.17 m (i.e., the test section should replace D5) to maximize the test time. In this case, Fig. 3 indicates that the arrival of the reflected shock will terminate a test that lasts about 4.8 ms. Similarly, for a nominal M_s of 1.95, placing the test section centerline at x = 4.58 (i.e., replacing D6 with the test section) corresponds to a maximum test time of about 2.7 ms.

Figure 4 shows the pressure time-histories during baseline shock tube tests that used both nominal burst disk pressures. Figure 4a corresponds to a shock Mach number of 1.68 and Fig. 4b corresponds to a shock Mach number of 1.94. The first increases in pressure mark the crossing of the incident

M_s	P_4, kPa	P_1, kPa	T_4, K	T_1, K	W_s, m/s
1.67 ± 0.03	1242 ± 45	82.5 ± 0.9	299.0 ± 0.6	296.7 ± 1.2	577 ± 10
1.95 ± 0.02	2935 ± 170	82.4 ± 1.0	300 ± 1.6	296.7 ± 1.3	673 ± 9
2.05 ± 0.02	4170 ± 350	83.2 ± 0.2	297 ± 1	296.3 ± 1.5	707 ± 3

Table 1: Baseline Shock Tube Experimental Conditions

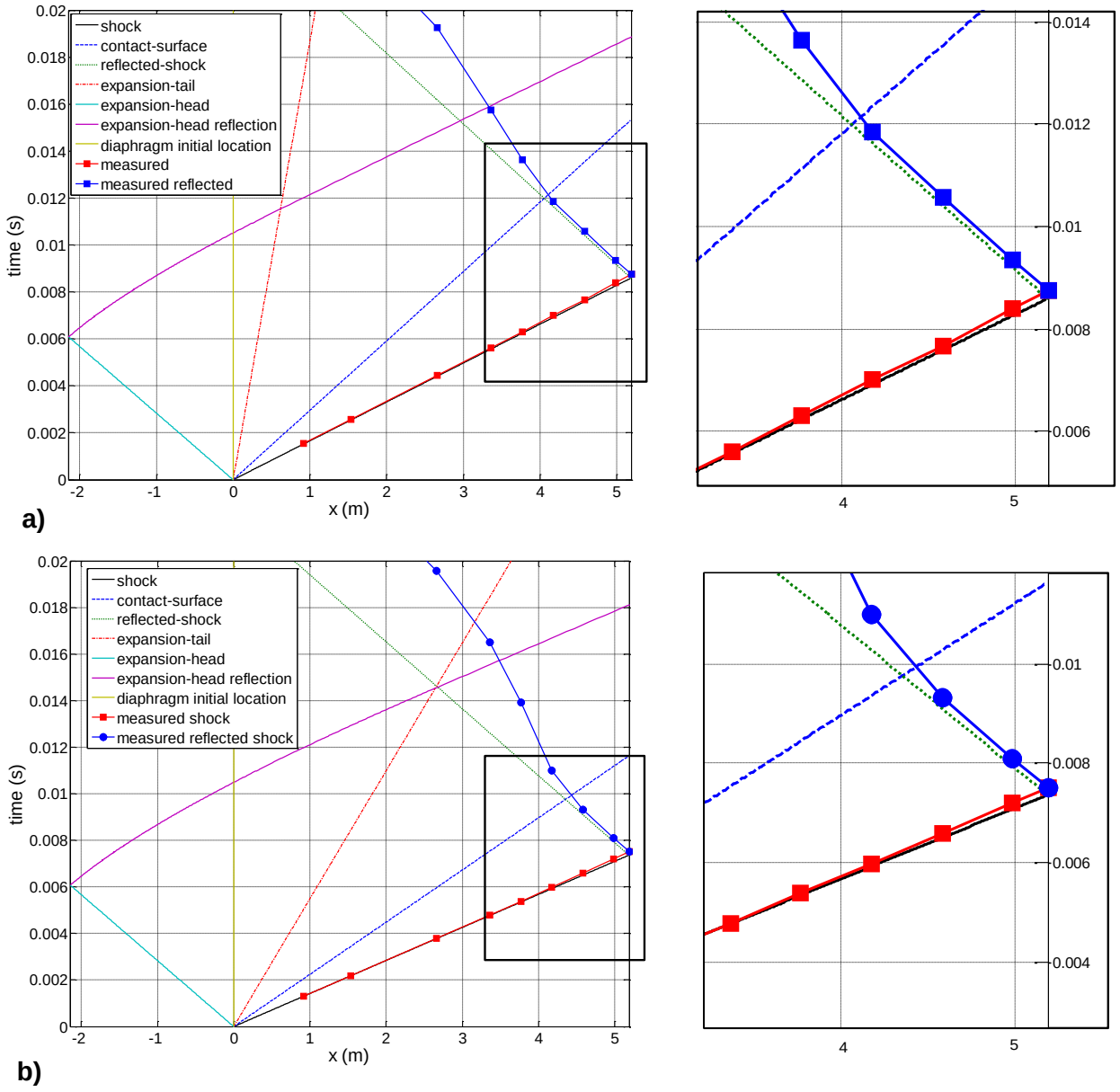

Fig. 3: *t-x* diagrams comparing measured shock crossing times to those predicted by ideal shock tube theory for two different shock Mach numbers. The insets to the right show more clearly the decay of shock velocity with distance: a) M_s = 1.66, b) M_s = 1.95.

shock over the sensors as it propagates downstream. Like Fig. 3, Fig. 4 shows shock attenuation, as is evidenced by the decreasing P_2 values with increasing streamwise distance. As expected, the reflection of the shock from the end wall at x = 5.19 results in a single pressure increase followed by a nearly constant pressure plateau. In Fig. 4a, the reflected pressure P_5 is about $8\ P_1$ compared to a theoretical [16] value of 9.5 P_1. Attenuation is also shown in Fig. 4b where the reflected pressure P_5 is about 13.1 P_1 compared to a theoretical value of 15.7 P_1. For both shock Mach numbers, a further increase above the reflected shock pressure is observed. In Fig. 4a, the end wall data show the pressure increases above the reflected value P_5 at a time of about 11 ms. A similar rise in the end wall pressure is seen in Fig. 4b at a time of about 9 ms. The percentage increases over the reflected shock pressures at M_s = 1.68, and 1.94, are 40%, and 95%, respectively. By comparing the times of the pressure increases to the times at which the contact surface appears to intersect the reflected shock in Fig. 3, it appears that an interaction of the contact surface with the reflected shock [17] is the cause of the increase. As previously mentioned, the components of the tube that limit the maximum allowable pressure are the last five driven sections. The peak pressure measurements were compared to the maximum pressures predicted by the shock-physics code CTH [18]. Using the same initial conditions as in the tests at M_s = 1.68, and 1.95, CTH predicted the peak pressures to be 14 and 32 P_1, respectively. Note that these values are about 20 to 25% higher than those measured. However, the shock-physics code does not include viscous effects, and thus the pressures it predicts are conservative from a design standpoint. The effects of the interaction of the contact surface and reflected shock are clearly not insignificant and thus must be considered prior to choosing a maximum driver pressure. Based on the peak pressures given by CTH simulations and the maximum allowable pressures of the last five driven sections, the maximum driver pressure is limited to about 4140 kPa (600 psig).

The use of multiple sensors at the same axial location allows for the planarity of the incident shock to be measured. As shown in Fig. 1, the four sensors in the sixth driven section (D6) and the three sensors in the driven end plate provide measures of shock planarity. In short, the four sensors in section D6 gave shock crossing times that were within 2.5 μs of one another. The same was true for the three sensors in the driven end plate. Note that 2.5 μs was the temporal resolution of the measurements since the data were sampled 400 kHz. Thus, the incident shock is considered to be well planar and therefore appropriate for testing its impingement on a dense gas-solid field of particles.

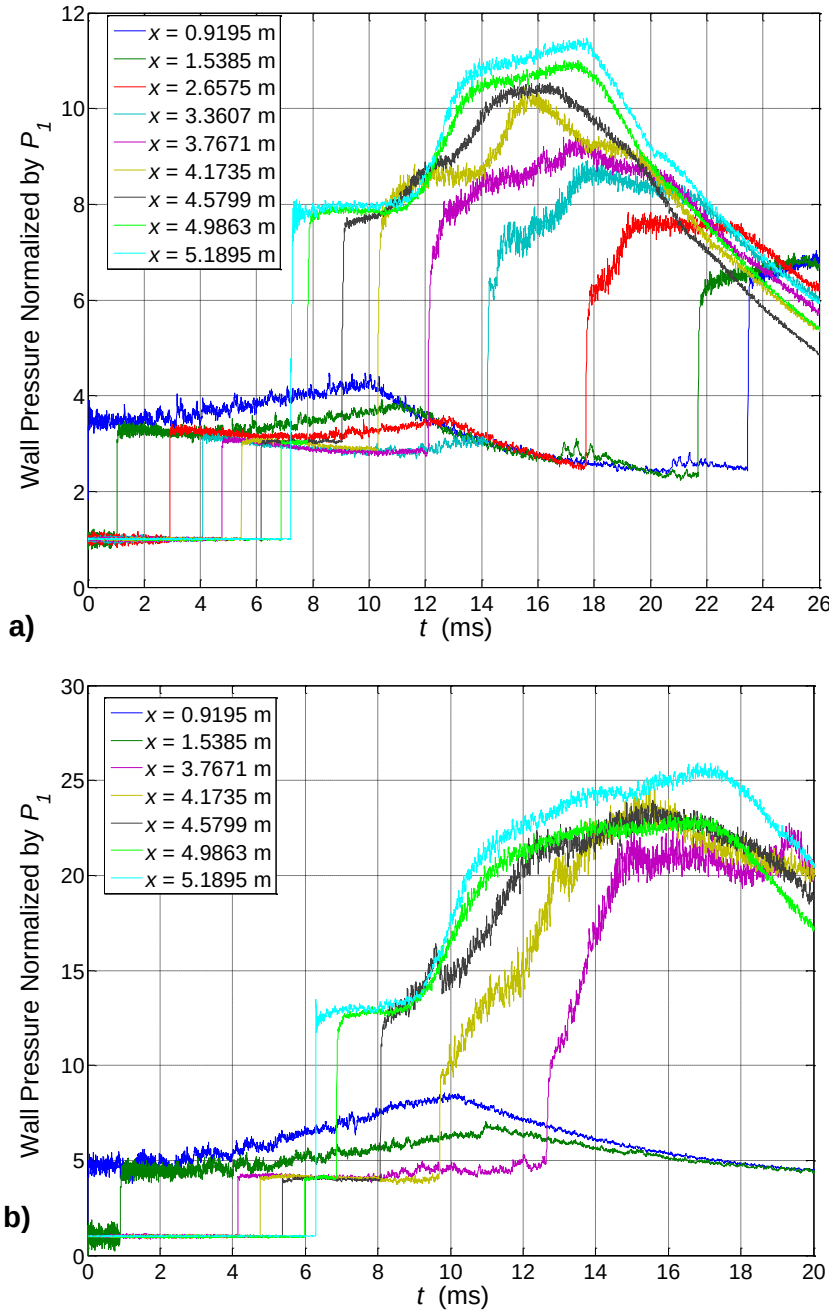

Fig. 4: Pressure time-histories during a shock tube test: a) M_s = 1.68, b) M_s = 1.94.

3. Dense Gas-Solid Flows

3.1. Benchtop Development of the Particle Curtain Concept

As discussed, the purpose and unique aspect of this shock tube facility is its ability to provide multiphase solid-gas flows within the dense gas volume fraction regime. The development of a method of suspending particles in the driven section was challenging owing to the relatively high particle volume fractions φ_p of about 1 to 50% required. One of the first ideas entertained for particle seeding involved using a fluidized bed such as in the dusty-gas experiments of Sommerfeld [19]. However, it was realized that it would be difficult to obtain high enough volume fractions using a fluidized bed seeder. In addition, there were concerns that a fluidized bed would not provide an isotropic distribution of particles, or maintain a constant particle flow rate. Furthermore, the use of a fluidized bed would result in the migration of particles throughout the driven section, which would be undesirable as it could alter the planar shock prior to its arrival at the test section. An alternative seeding method was developed with bench-top experimentation. The successful concept that emerged for particle seeding was that of a gravity-fed "particle curtain", or particle "rain."

Figure 5 shows a schematic of the apparatus used to develop the particle curtain concept. The particles are spherical soda lime particles having diameters of about 106-125 μm. The relatively narrow particle size distribution is obtained using appropriately sized sieves. An acrylic tube with an internal diameter of 63.5 mm serves as the particle reservoir. Prior to a test of the particle curtain apparatus, the particles are loaded into the upper reservoir where they rest on a gate valve. As demonstrated in Fig. 5b, upon opening of the valve, the particles fall into the lower reservoir and begin to flow through the 3.2 mm wide thick slit plate at the bottom of the lower reservoir. As

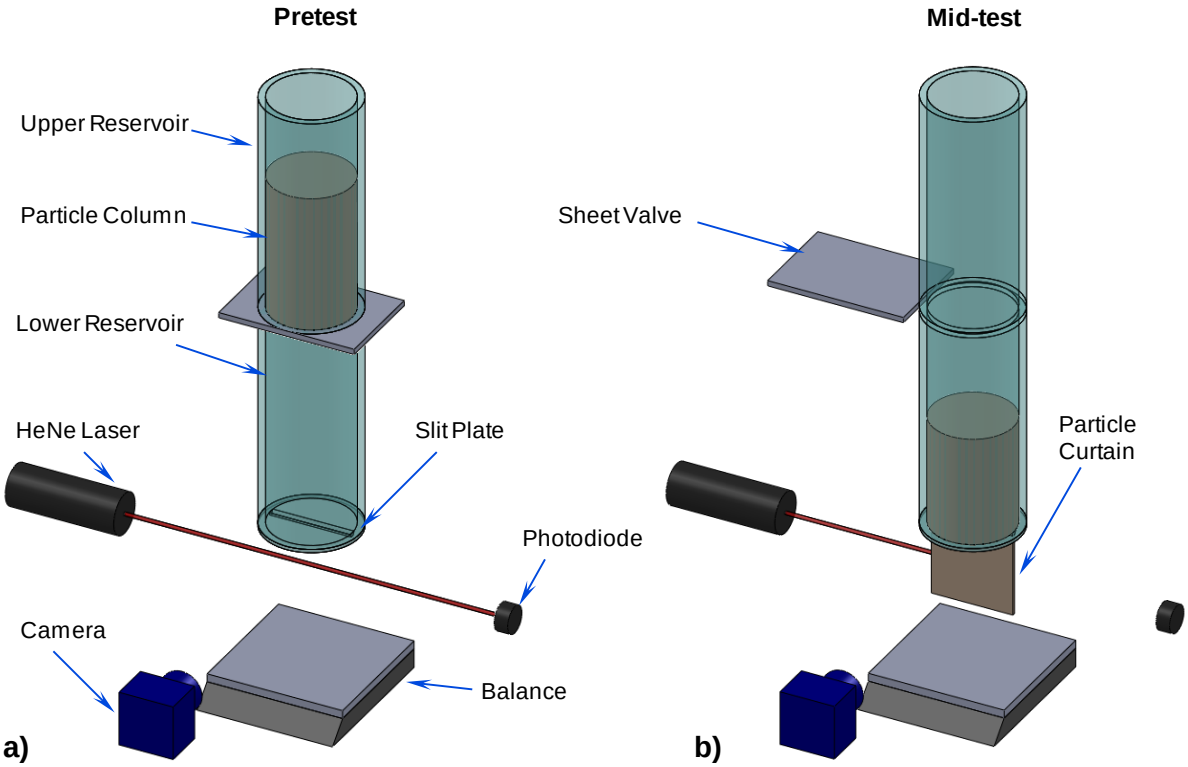

Fig. 5: Schematic showing the table-top apparatus used to develop and test the particle curtain concept: a) prior to a test, and b) during a test.

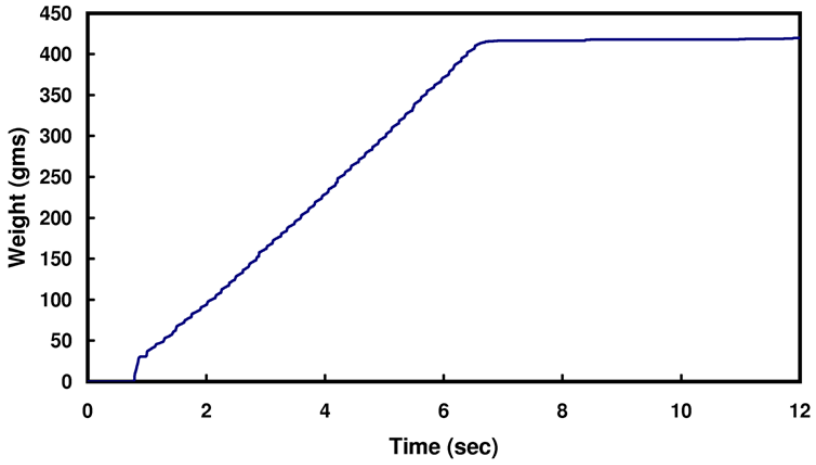

Fig. 6: Plot of mass flow of curtain versus time for 3.2- mm width slit.

illustrated in Fig. 5, the interruption of a HeNe laser signal on a photodiode triggers a strobe lamp and a camera (AOS Technologies X-Motion) to acquire images of the flowing particle curtain at 500 Hz. The images are used to measure particle velocities, which are about 1 m/s. In addition, a computer-controlled precision balance (Mettler Toledo X5400S2) dynamically measures the accumulated weight of the particles passing through the slit. From the particle mass flow rate, particle velocities, and known total volume that the particle curtain occupies, the particle volume fraction is determined.

Different slit geometries were tested in order to find a configuration that provided a nearly constant particle flow rate. It was found that adding a bevel of about 60-degrees to the slit plate helped stabilize the particle flow and maintain a smooth, nearly constant particle flow rate. In addition, the bevel was seen to increase the mass flow by about 15% and it also prevented the particles from building up near edges of the slit entrance. Three different beveled-slit geometries having different slit widths were developed and tested. Varying the slit width was seen to vary the particle flux through the slit. Therefore, the particle volume fraction could be controlled according to the slit width. Three different slits, having widths of 1.6 mm, 3.2 mm, and 4.8 mm, were utilized to provide curtains with particle volume fractions φ_p of 3%, 16%, and 35%, respectively. Each of the three slit geometries provided near constant particle flow rates. As an example, Fig. 6 shows a plot of particle mass versus time using the 3.2 mm wide slit. The figure demonstrates that after about 1 second, the mass flow rate of the particle curtain is nearly constant until about 6 seconds. Finally, Fig. 7 shows a backlit image of the flowing 3.2 mm-wide particle curtain. The figure demonstrates that the distribution of particles is nearly spatially isotropic.

3.2. The Particle Curtain Test Section

Figure 8 shows a schematic of the particle curtain test section installed in the shock tube in order to test the impingement of a planar shock on a dense field of particles. The inner width of the test section is 79.2 to match the adjacent driven sections. The particle curtain reservoir is similar to the bench-top apparatus described above, but it is now a pressure vessel that is designed to contain the particles following shock impingement. Figure 9 shows a closer view of the test section with both a schematic and photo. The sidewalls are also designed to accept small glass (BK-7) windows having dimensions of 88.9 mm × 88.9 mm × 12.7 mm. These windows are commercially available from ESCO Products, and are relatively inexpensive, which is desirable since they might require frequent replacement owing to damage from the particles. Backing supports are used, which reduce the window viewing area to a 50.8 mm diameter circle. An aluminum particle reservoir, having an inner

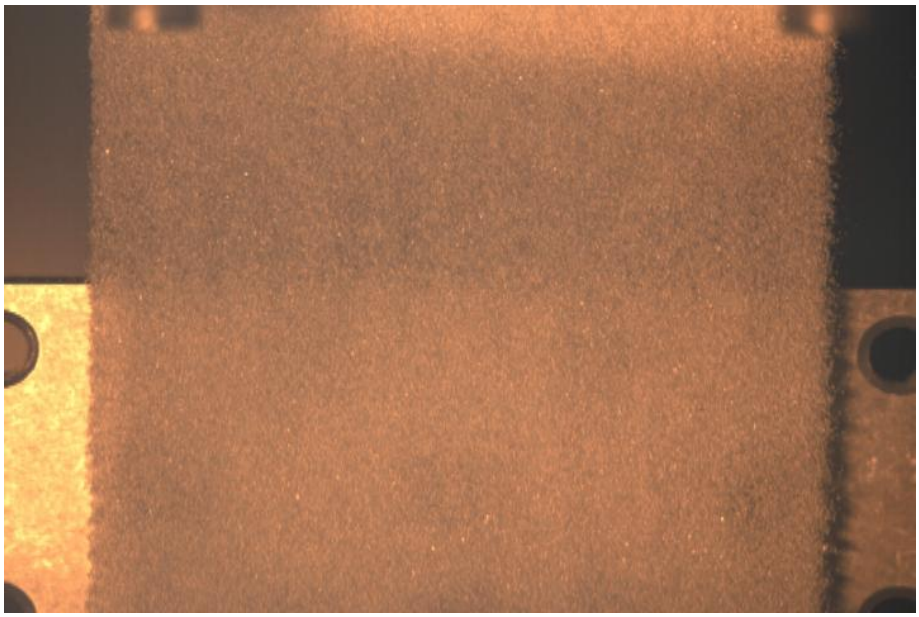

Fig. 7: Backlit image of the 3.2 mm-wide particle curtain.

diameter of 76 mm, is used to initially store spherical soda lime particles that have diameters of 106-125 μm. Prior to an experiment, the soda lime particles rest on an initially closed industrial gate valve (Salina Vortex Model SA06-MG-RS). During a test, but prior to the rupture of the burst disk, the gate valve opens beginning the flow of particles into the test section. The particles flow through a beveled slit reaching a nearly constant flow rate in less than one second. The particles exit the test section through a slit in the floor and then enter a particle collector reservoir, which contains an internal funnel and a ball valve to empty the particles after a test.

Figure 10 shows a schematic of the test section with the particle reservoirs removed. Figure 10a is a top view of the test section demonstrating the slit geometry used to form the gravity-fed particle curtain. In the figure, the slit is spanwise parallel, but the ceiling insert can be turned 90-degrees to produce a streamwise parallel particle curtain. The ceiling slit insert contains a 60-degree bevel with respect to the *x* direction. As described above, the bevel serves to stabilize the particle flow producing a nearly steady state flow. The spanwise width of the slit is 68.6 mm, or about 87% of the full span of the test section. The streamwise thickness of the slit is 3.2 mm. As is seen in Fig. 10b, the test section sidewalls are also designed to accept large glass (BK-7) windows with viewable dimensions of 254.2 mm × 76.2 mm and thicknesses of 31.8 mm. Finally, Fig. 10c gives a side-view of the ceiling slit insert to demonstrate the geometry used to produce the nearly spatially isotropic particle curtain.

The gravity-fed seeding apparatus serves to shape the particles into what is termed the "particle curtain." Figure 11 shows a photo of the spanwise curtain as installed in the test section; the photo was acquired at an oblique angle with a test section wall removed. The photo demonstrates that the curtain is locally spatially isotropic. The curtain narrows to a streamwise thickness of about 2.2 mm for the bottom 75% of the test section height and there is some variation in particle volume fraction with height owing to gravity. The volume fraction of the curtain varies approximately linearly from about 24 ± 2% at the ceiling to about 13 ± 2% at the floor. The volume fraction at the center is about 19 ± 2%. The particles flow at a velocity of about 1 m/s, which makes them essentially frozen compared to the shock velocities.

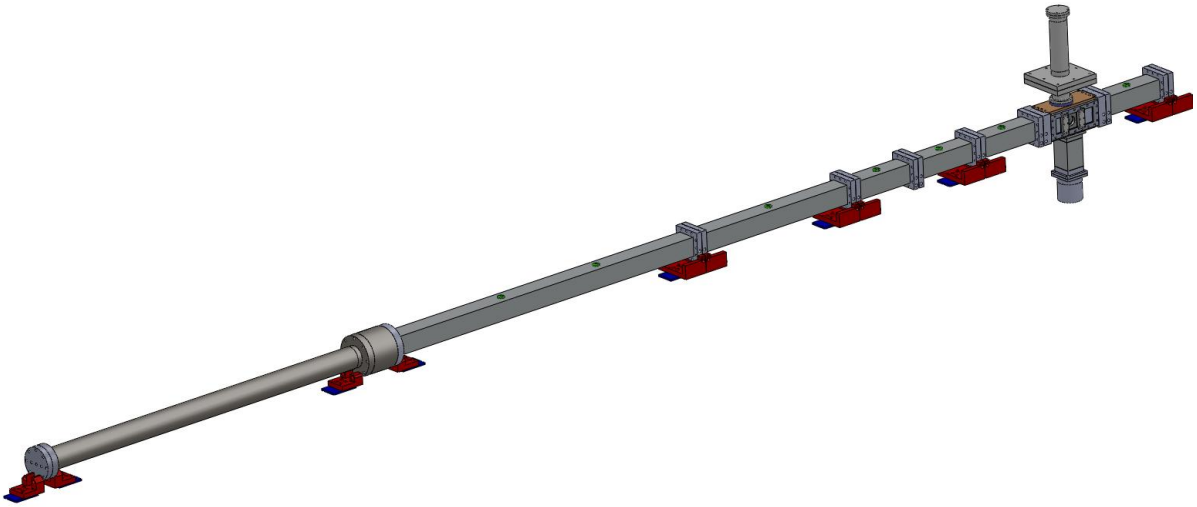

Fig. 8: Schematic of the multiphase shock-tube.

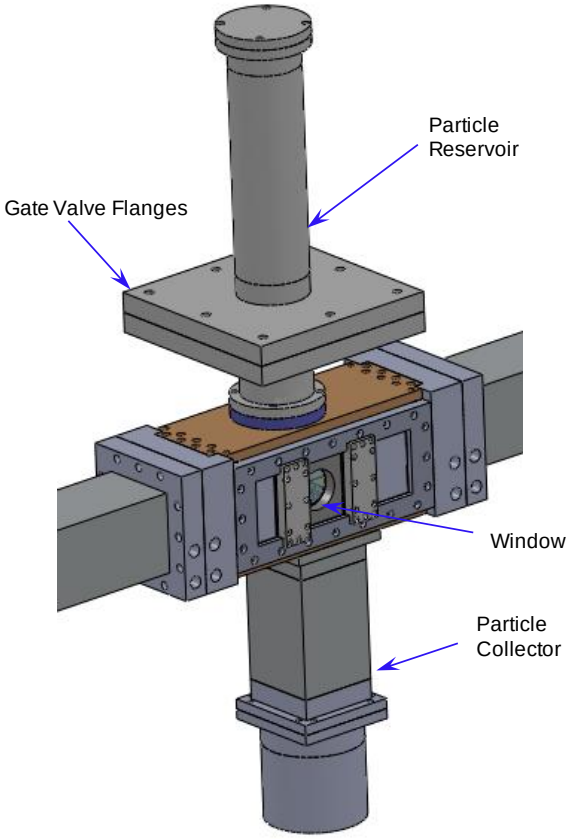

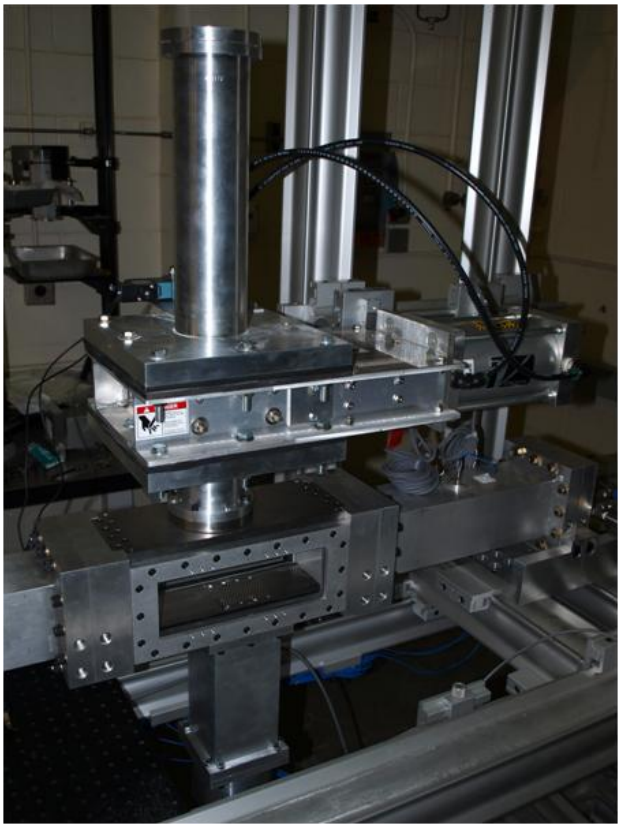

a) **b)**

Fig. 9: Particle Curtain Test Section: a) Schematic showing the particle curtain test section with the sidewalls containing small windows, and b) Photo showing the test section outfitted with large windows.

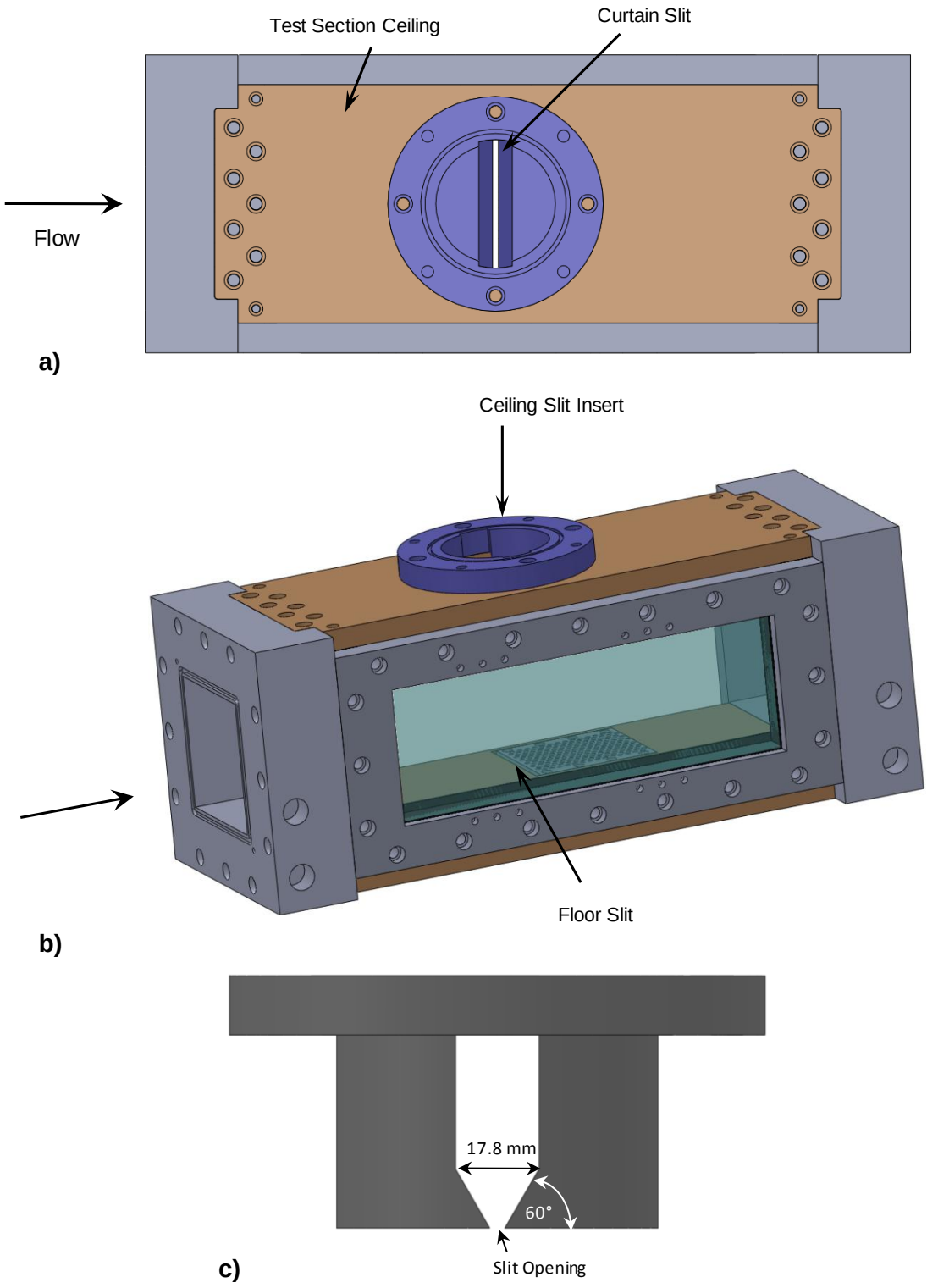

Fig. 10: Schematics showing further details of the particle curtain test section: a) top view to demonstrate the curtain slit geometry, b) isometric view with the sidewalls containing large windows, and c) side-view of the ceiling slit insert (Note the test section ceiling surrounds the insert to contain the particles so that the only particle exit is through the slit).

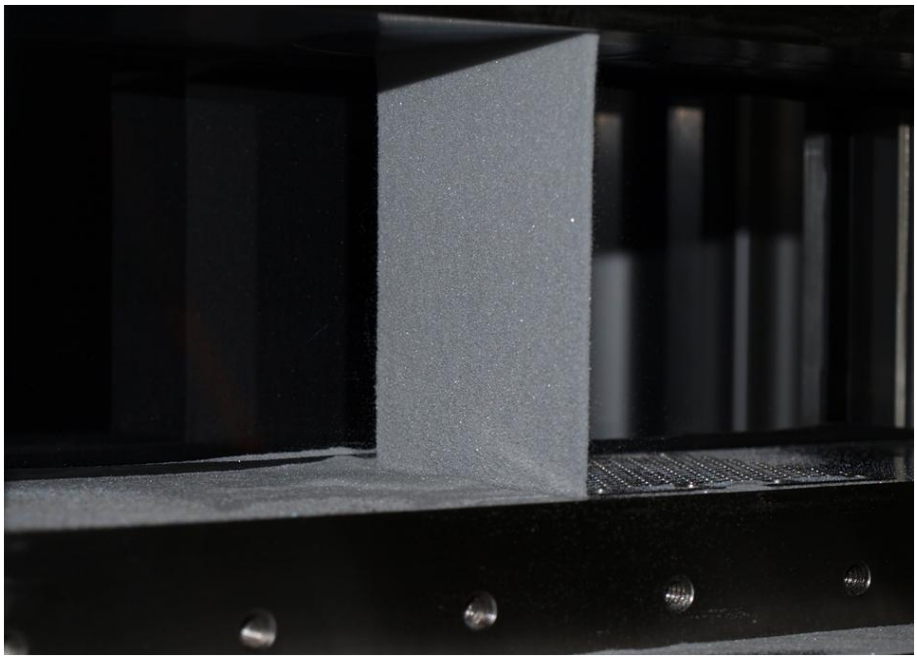

Fig. 11: Photo of the particle curtain acquired with a test section wall removed.

3.3. High-Frequency Pressure Instrumentation

The same type of fast-response PCB pressure transducers used for measurement in the baseline shock tube were employed for the particle curtain interaction experiments, except that additional sensor locations were used. The sensor diameter is about 5.6 mm. The sensors have a manufacturer specified bandwidth and rise time of 500 kHz, and 1μs, respectively. However, owing to the finite sensor size (and therefore finite shock crossing time), the effective rise time of the sensors for the shocks herein has been measured to be about 3-5 μs (depending on shock speed). Two signal conditioner boxes (PCB Model 483C) provide the transducers the constant current, excitation voltage, and signal amplification necessary for operation. The amplified signals are low-pass filtered (Krohn-Hite Model 3944) with a cutoff frequency of 1 MHz. The filtered signals are then sent to a data acquisition chassis (NI PXI 1505), in which two data acquisition cards (NI PXI 6133) digitize the signals at a sampling frequency of 2.5 MHz. The digitized signals travel through fiber optic cables to a personal computer where they are recorded. As shown in Fig. 1, a sensor approximately 1 meter downstream of the burst disk provides a trigger signal for both the pressure and imaging data acquisition. In addition, a sensor about 0.4 meters downstream of the interaction is used to measure the shock attenuation associated with the interaction.

An additional array of seven sensors was constructed to capture the pressures immediately downstream of the curtain. This is shown in Fig. 12. These sensors are usefully located to study the interaction of the incident shock with the particle curtain. As also can be seen in Fig. 12, the coordinate system in Section 3 is defined to originate at the upstream edge of the curtain, at the floor, and at the spanwise center of the curtain. The pressure sensors are placed 13.3, 43.8, and 64.1 mm downstream of the curtain. In order to capture spanwise variations of the interaction, sensors are placed along the z axis from z = -20.3 to +20.3 mm. Pressure data from this sensor array are given in Section 3.5 below.

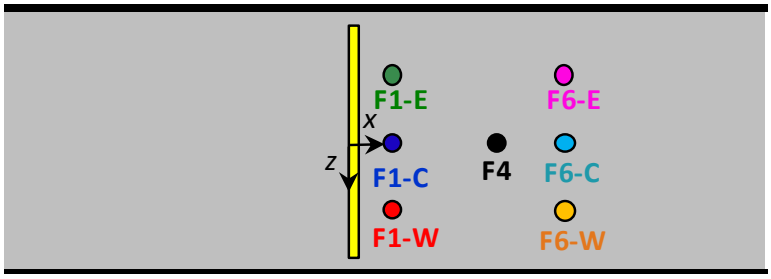

Sensor Number	Location (x, z) mm
F1-E	(13.3, -20.3)
F1-C	(13.3, 0)
F1-W	(13.3, 20.3)
F4	(43.8, 0)
F6-E	(64.1, -20.3)
F6-C	(64.1, 0)
F6-W	(64.1, 20.3)

Fig. 12: Coordinate system and floor pressure sensor locations. The yellow rectangle denotes the particle curtain and y = 0 is along the floor.

3.4. High-Speed Schlieren Imaging

A high-speed schlieren imaging system is used to study the wave structure and particle motions that occur following the impingement of a planar shock on the particle curtain. The light source is a Visual Instrumentation Corporation continuous-wave high brightness LED (Model 900415). The images are acquired with a Phantom digital camera (v12.1) having a resolution at full-frame of 1280 × 800 pixels. Figure 13 shows the two different schlieren imaging fields of view that were used in this study. The smaller view (50 × 25 mm^2) was used to acquire images near the center of the test section. The framing rate was 130 kHz and the image resolution was 256 × 128 pixels. To collimate the source for this case, a 50.8 mm diameter biconvex lens with a focal length of 2 m was used. To focus on the knife-edge, a 50.8 mm diameter plano-convex lens with a focal length of about 0.8 m was used. A larger field (100 × 64 mm^2) was utilized to obtain images that spanned from the floor to about 80% of the test section height. The framing rate for the large field of view was 41 kHz and the image resolution was 512 × 256 pixels. The optics used were 101.6 mm diameter plano-convex lenses with a focal length of 2 m. The resulting schlieren images are presented in Section 3.5 below.

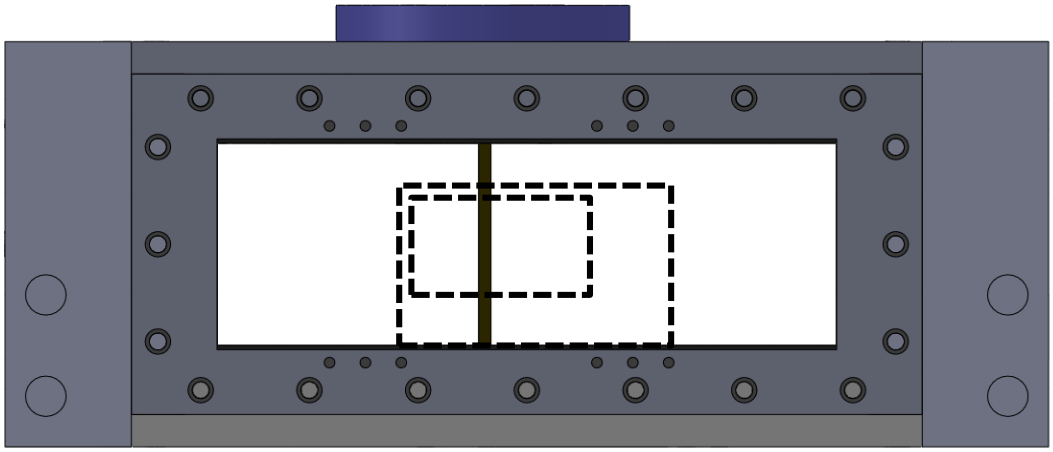

Fig. 13: Schlieren fields of view. The solid rectangle denotes the 3.2 mm thick particle curtain. The smaller dashed rectangle gives the 50 × 25 mm^2 viewing area of the images in Fig. 14, and the larger dashed rectangle gives the 100 × 64 mm^2 viewing area for the images in Fig. 16.

3.5. Results and Discussion

The test conditions for the particle curtain experiments were slightly different than those for the baseline shock tube given in Table 1. The differences are likely attributed to different test section hardware and different measurement stations for determining shock crossing times. Experimental test conditions acquired for all three shock Mach numbers are presented in Table 2. The velocity of the shock W_s is measured using shock crossing times obtained from two ceiling mounted sensors upstream of the test section center at x = -69 mm and at x = -388 mm. Again, x = 0 corresponds to the initial upstream edge of the curtain in this section. The shock Mach number M_s is calculated based on the initial temperature of the driven gas T_1 and its speed of sound assuming a calorically perfect gas. The ranges of the experimental parameters presented in Table 2 are 95% confidence bands that are based on student-t theory.

Figure 14 shows schlieren frames of the interaction of a Mach 1.66 incident shock with the particle curtain. As labeled in Fig. 13, the image field of view is 50 × 25 mm^2 and near the center of the test section. The sequence of images was chosen from a 130 kHz movie and the flow is from left to right. The exposure time in each image is one microsecond. The first impact of the incident shock on the curtain is defined to be t = 0. At t = -10μs, the 2.2 mm thick curtain is near the center of the image along with some extraneous particles that have escaped the bulk curtain flow. The incident shock has propagated into the field of view and is about 6 mm upstream of the initial curtain. Five μs after impact, transmitted and reflected shocks are observed. From t = 5 to 31 μs, the reflected shock and transmitted shock travel through the field of view. As the transmitted shock travels downstream, it appears to broaden, which is likely an indication that there is spanwise curvature and/or possibly rippling of the shock. Some shock curvature is to be expected considering that the initial curtain spans

M_s	P_4, kPa	P_1, kPa	T_4, K	T_1, K	W_s, m/s
1.66 ± 0.02	1242 ± 45	82.7 ± 1.6	298 ± 2	296.4 ± 1	568 ± 15
1.92 ± 0.03	2935 ± 170	82.7 ± 1.6	299 ± 2	296.4 ± 1	671 ± 13
2.05 ± 0.02	4170 ± 350	82.7 ± 1.6	297 ± 1	296.4 ± 1	696 ± 8

Table 2: Particle Curtain Shock Tube Experimental Conditions

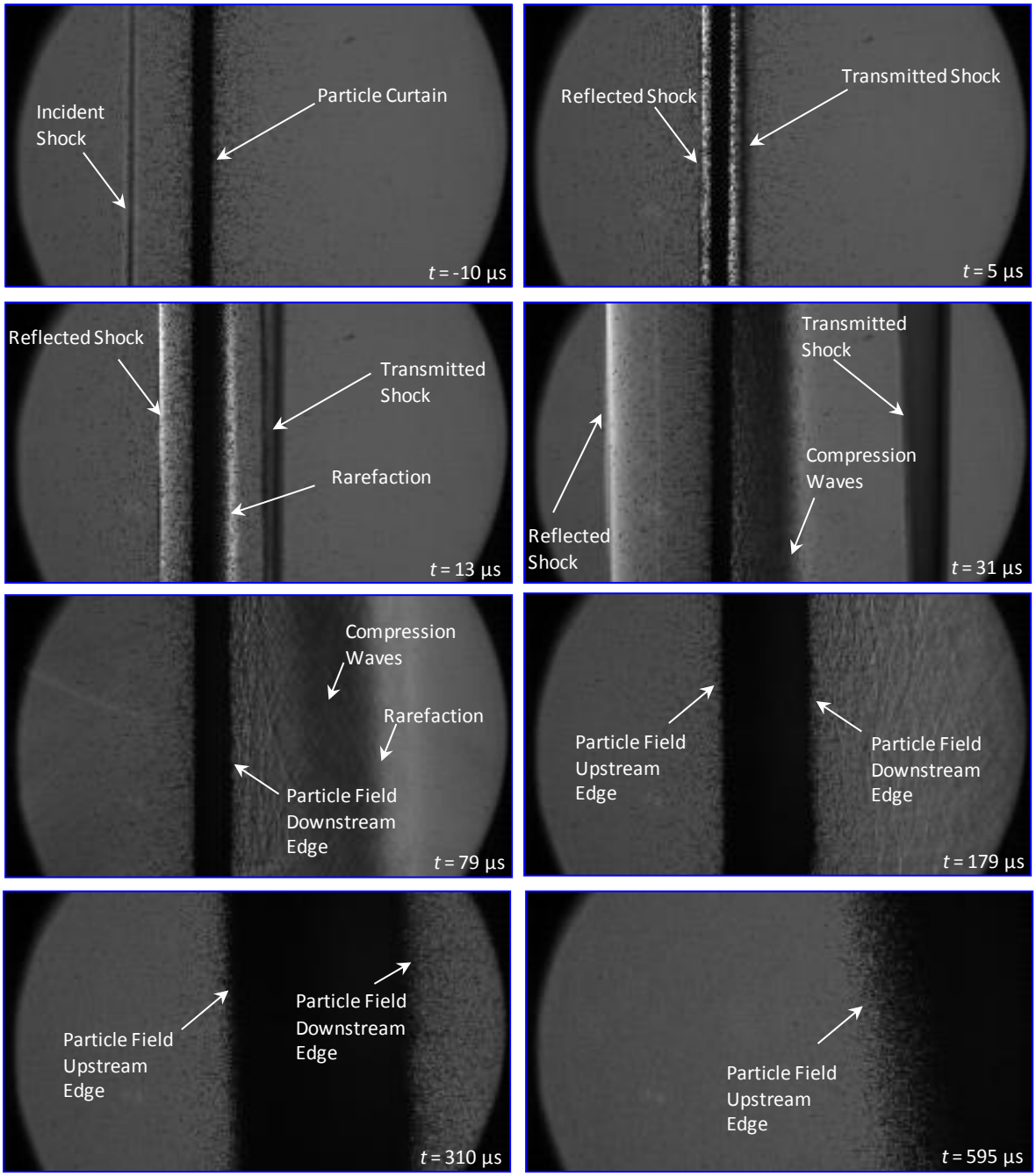

Fig. 14: Schlieren images showing the first 595 µs of the interaction of a M_s = 1.66 incident shock with the particle curtain. The images were acquired with a vertical knife edge to highlight horizontal gradients. The images were acquired near the center of the test section at a framing rate of 130 kHz. The exposure time of each image was 1 µs.

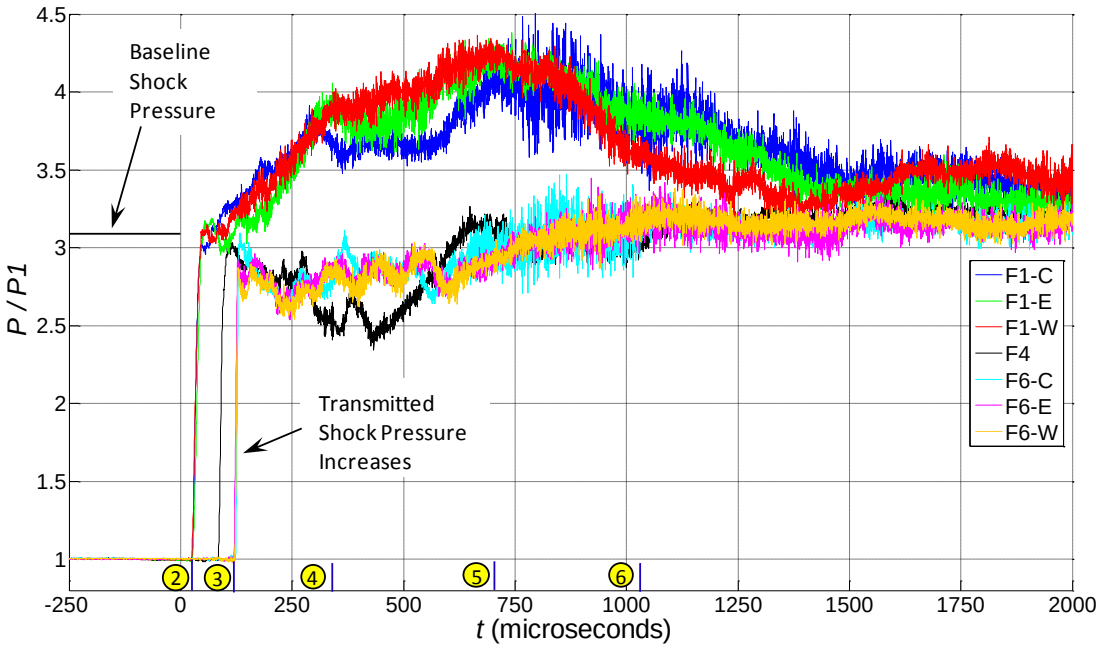

Fig. 15: Floor pressures during the interaction of a M_s = 1.66 incident shock with the particle curtain. Note that the pressure ratio across the baseline shock (without a particle curtain) is about 3.1. The yellow numbers just above the time axis correspond to the labels in the images of Fig. 16, which were acquired on the same test.

about 87% of the test section width. In the t = 13 μs image pronounced rarefaction waves emanate from the curtain. With continuing time, the rarefaction propagates downstream and spreads. The rarefaction is similar to that which follows a detonation front. Since the interaction involves a transmitted and a reflected shock, flow properties such as pressure and velocity will initially vary across the curtain. These differences are quantified further below. At t = 31 μs, smooth compression waves propagate downstream away from the particle curtain. These compressions likely occur as the pressure across the curtain begins to equilibrate.

Although not shown here, the first motions of the curtain are observed around 40 μs. At t = 79 μs, it can be seen that the downstream edge of the particle curtain has translated. With continuing time, the upstream edge of what was initially the particle curtain also travels downstream. However, the upstream edge velocity is lower, resulting in the spread, or dispersion, of particles into what is denoted a "particle field." Following the impact of a planar shock on a granular bed of particles, Rogue et al. [12] also noted the spread, or "dilution" of the particles as they traveled downstream. The particle field continues to disperse between the images acquired at t = 79 and 310 μs. At t = 595 μs, the downstream edge of the particle field has propagated out of the field of view, but the upstreamedge is still visible. Although not shown here, the entire particle field propagates out of the field of view at about t = 800 μs.

Floor pressures during a M_s = 1.66 interaction are presented in Fig. 15. In addition, Fig. 16 presents simultaneous schlieren frames from a 41 kHz movie during the interaction acquired in a larger 100 × 64 mm^2 field of view. As seen in Fig. 13, the image encompasses about 80% of the total test section height and it includes the floor. The locations of the floor sensors are given in Fig. 12. For comparison purposes, the streamwise location of the sensors is annotated at the bottom of each schlieren image in Fig. 16 and the time of each image is marked with a line in Fig. 15. The yellow numbers next to the time lines in Fig. 15 correspond to those labeled in the images of Fig. 16. The images in Fig. 16 show the first millisecond of the interaction. The first image shows that downstream

of the curtain is a particle hill with a height of a few millimeters. The extraneous particle buildup occurred during the transient start up of the particle seeder and is unavoidable with the current design. However, the buildup has not been observed to significantly affect the interaction. Alternative designs were considered that included a wider floor slit, or a perforated floor, but evidence suggests that either of these options would do more to disturb the shocks than the slight particle buildup. At t = -1.6 μs, the incident shock is just upstream of the curtain. The next frame of the movie, at t = 23 μs shows the transmitted and reflected shocks as well the rarefaction and compression waves that were observed in Fig. 14. The transmitted shock has not yet crossed the three F1 sensors located at x = 13.3 mm. Owing to the particle hill, the transmitted shock exhibits some curvature near the floor. The next image at 121 μs after impact shows the transmitted shock has again appeared to broaden indicating a spanwise curvature, and/or rippling of the shock has occurred. Inspection of frames in between 23 and 121 μs (not shown here) showed that the shock broadening increases as it moves downstream.

Figure 15 shows the sharp pressure increases associated with the passage of the transmitted shock. At the sensors immediately downstream of the curtain (x = 13.3 mm), the transmitted shock raises the pressure to about 3.1 P_1, which is close to the baseline (without particles) case. Much different from the baseline case, the pressures continue to increase following the passage of the transmitted shock. The first pressure increases above the transmitted shock levels are due to the propagation of the smooth compression waves seen in Fig. 16. Rogue et al [12] measured similar downstream propagating compressions. The pressure then continues to increase as the particle field moves over the sensors. For example, the fourth image of Fig. 16, acquired at t = 340 μs, shows the particle field to be over the F1 sensors. Comparison to Fig. 15 shows that the pressures increase as the particles convect over the sensors. This indicates that there is still quite a large pressure difference across the particle field at x = 13.3 mm. In a sense the field acts as a porous wall, through which the pressure equilibrates through the mechanism of flow between the particles. At t = 705 μs, the particle field has crossed x = 13.3 mm entirely, which results in more constant pressures at the F1 transducers. The pressures reach a peak value that is about 1/3 greater than in the baseline case. The pressures at the F6 sensors (x = 64.1 mm) have begun to increase as the downstream edge of the particle field has crossed over them. However, the pressure increase associated with the particle field is much smaller at x = 64.1 mm. This implies that the pressure equilibrates across the particle field as it spreads and propagates downstream. Beginning at about 800 μs, the pressures at x = 13.3 mm begin to decrease. Since the particles are now downstream of the sensors, rarefactions propagate upstream as the pressure continues to equilibrate. Rogue et al [12] also noted rarefactions to propagate upstream following the impact of an incident shock on a particle bed. Finally, the last image in Fig. 16, acquired at t = 1022 μs, shows that the particle field is nearly out of the field of view. Figure 15 indicates that as time progresses from 1 to 2 ms, the pressures in the test section equilibrate.

Pressures upstream of the same M_s = 1.66 interaction are given in Fig. 17. The data were acquired on the same test as that of Fig. 15 and Fig. 16. Two upstream plots of pressure at x = -99.1 and -68.6 mm are shown. The incident shock results in the first sharp increases in pressure. The curtain shock reflection crosses x = -68.6 mm at about 305 μs and then x = -99.1 mm at about 463 μs. Following the pressure increases, rarefactions decrease the pressure. The rarefaction waves are likely a result of the pressure equilibrating across the curtain. At x = -68.6 mm, the pressure increases to about 4.3 P_1 which is an increase of about 1.4 times greater than the incident pressure. From this pressure ratio and one-dimensional unsteady wave theory, the reflected shock Mach number is about 1.16. The velocity downstream of the reflected shock then computes to be about 200 m/s. Figure 9 also shows that the reflected shock strength decreases as it propagates upstream. For example the reflected to incident pressure ratio at x = -99.1 is about 1.29, which gives a reflected shock Mach number of about 1.12. It is likely that the rarefactions that propagate upstream of the particle field serve to weaken the reflected shock [12]. Since the shock reflection slows as it propagates upstream, it is likely that the flow velocity just upstream of the curtain is lower than 200 m/s just after the impingement of the incident shock. Figure 15 shows that just downstream of the curtain, the transmitted shock pressure ratio is about 3, which gives a transmitted shock Mach number of about 1.65. The induced flow

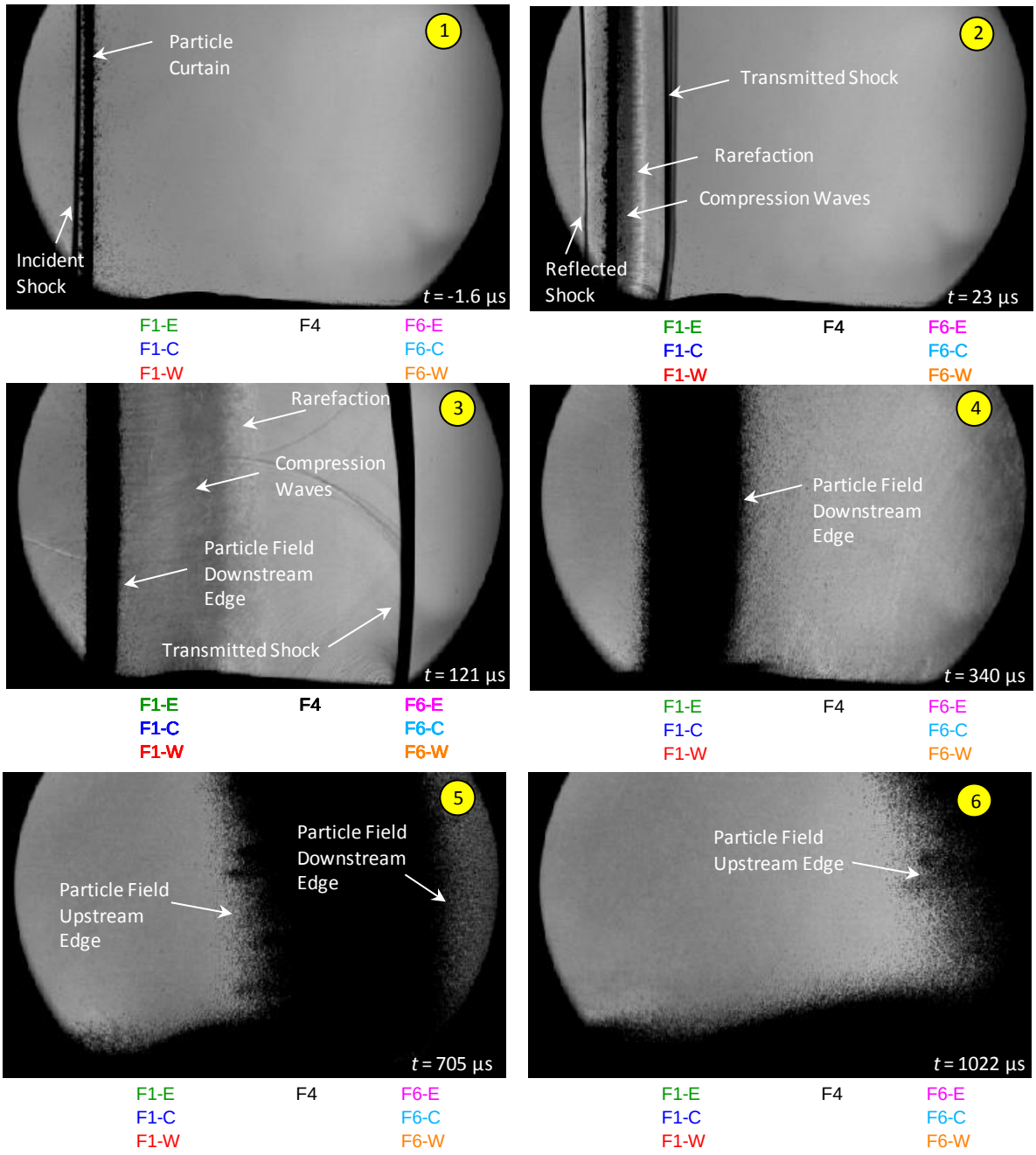

Fig. 16: Schlieren images showing the first 1 ms during the interaction of a M_s = 1.66 incident shock with the particle curtain. The locations of the floor pressure transducers are annotated at the bottom of each image for comparison to the pressure time-traces given in Fig. 15.

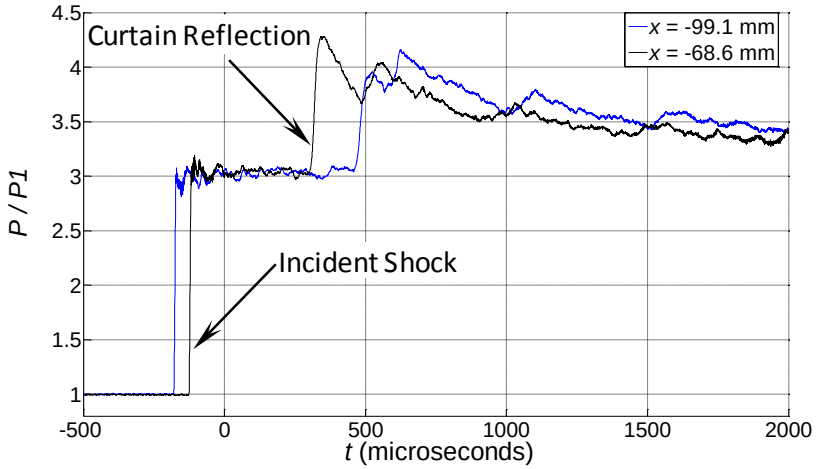

Fig. 17: Pressures upstream of the interaction of a M_s = 1.66 incident shock with the particle curtain. The pressures are during the same test as that in Fig. 15 and Fig. 16.

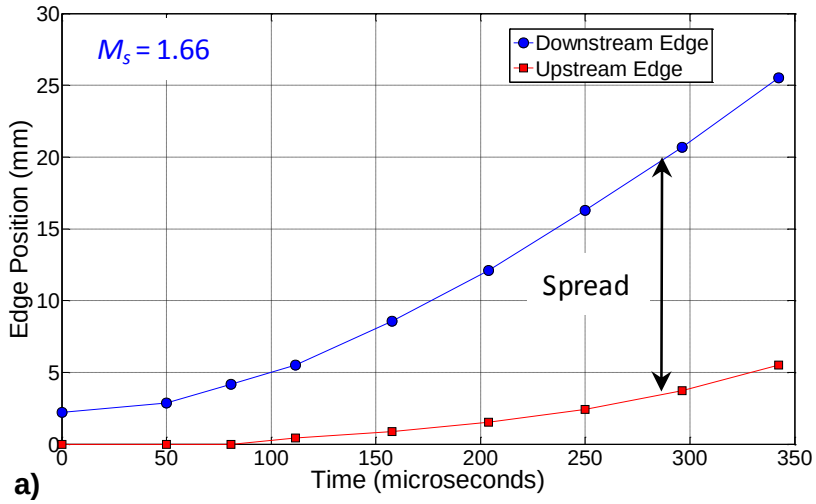

a)

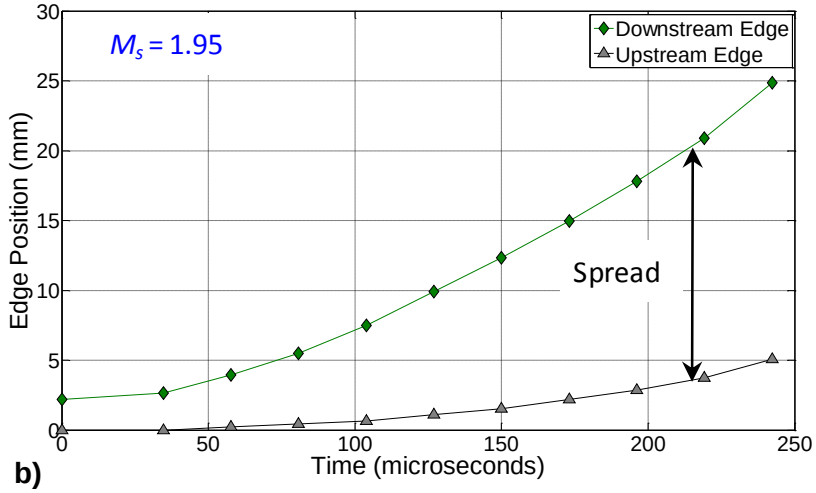

b)

Fig. 18: Upstream and downstream particle edge trajectories: a) M_s = 1.66, and b) M_s = 1.95.

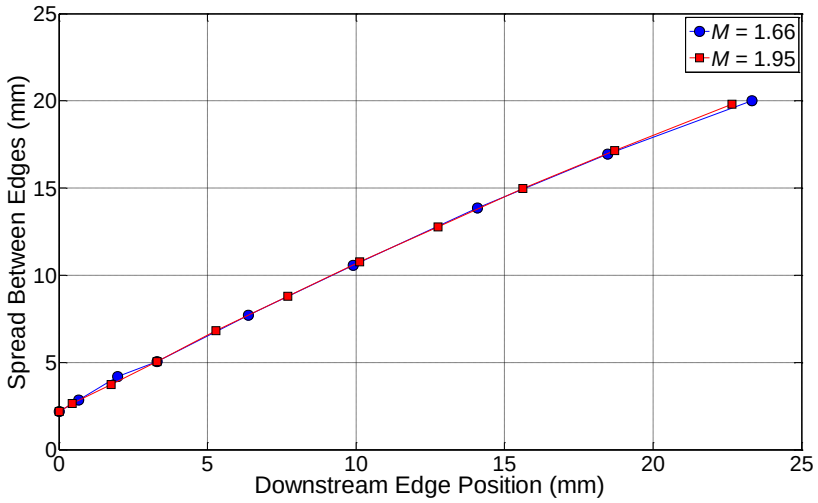

Fig. 19: Particle spread as a function of downstream edge position.

velocity behind the transmitted shock computes to about 300 m/s. Therefore, following the impact of the incident shock on the curtain, the velocity difference across the curtain is of order 100 m/s. This velocity difference leads to a difference in particle drag across the curtain and thus contributes to the spreading of the particle field observed in the schlieren movies.

Schlieren movies and fast-response pressure data were also acquired for the interaction involving an incident shock at M_s = 1.95. The images were observed to be qualitatively very similar to that seen in Fig. 14 and thus for the sake of brevity are not included. Like the M_s = 1.66 case, the pressure measurements showed that the M_s = 1.95 interaction resulted in peak pressures above that of the baseline when the particle field propagated over the sensors located at x = 13.3 mm. However, the peak pressures measured to be about 46% higher than the baseline, compared to about 35% for the lower strength incident shock.

Figure 18 shows particle edge trajectories for the M_s = 1.66 and the M_s = 1.95 interactions. The data, determined from the schlieren imaging, show the positions of the upstream and downstream edges of the particle fields as a function of time. The particle edge positions are those at the wall-normal centerline. In both cases the downstream edge propagates faster than the upstream edge resulting in the spread seen in the schlieren images in Fig. 14 and Fig. 16. The particles travel faster in the M_s = 1.95 interaction, which is to be expected. Interestingly, at a given particle edge position, the spread looks very similar in both cases. This is further quantified in Fig. 19, which shows the spread of the curtain with respect to the position of its downstream edge. The figure demonstrates that the spread of the particles, as a function of the distance traveled by the downstream edge, is essentially identical for both shock Mach numbers.

More complete descriptions of the trajectories of the upstream and downstream edges of the particle fields at three shock Mach numbers for four runs each are shown in Fig 20a and Fig. 20b, respectively. These plots include repeated shock tube runs for each Mach number, as well as a third Mach number of 2.01. Not surprisingly, both edges travel faster as the incident shock Mach number is increased. Dimensional analysis suggests that the trajectories could exhibit similarity if they are normalized by the incident shock induced velocity u_p. The resulting normalized trajectories are shown in Fig. 21, where the variables of both axes have also been divided by the initial streamwise thickness of the curtain h. Indeed, Fig. 21 demonstrates that when scaled by the post-shock gas velocity, the particle field trajectories collapse to a single curve. In the downstream edge plot of Fig. 21b, although

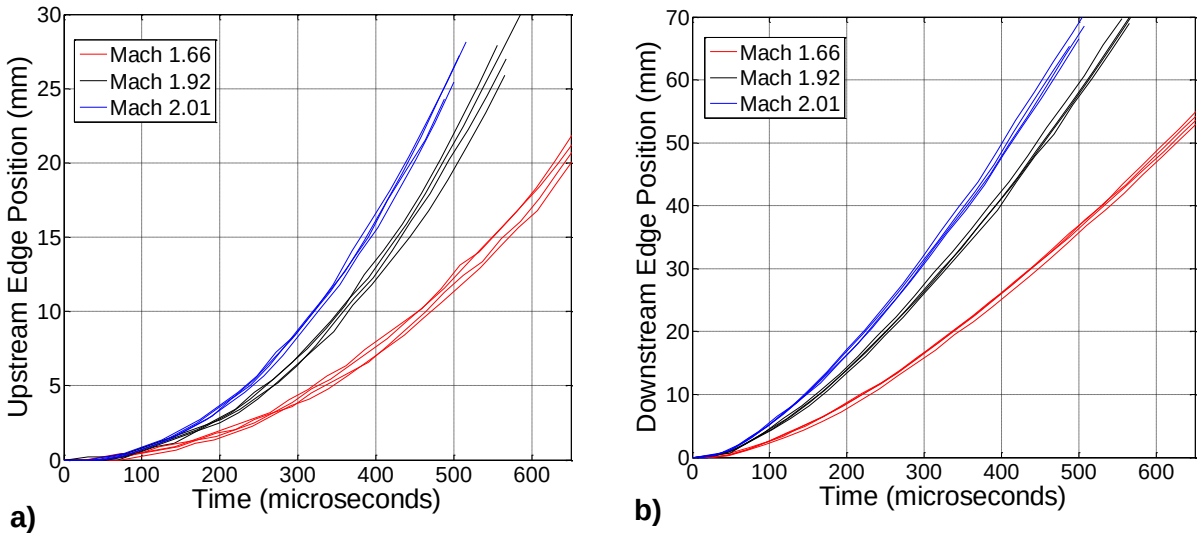

Fig. 20: Trajectories of the particle field edges as determined with high-speed imaging: a) upstream edge, and b) downstream edge.

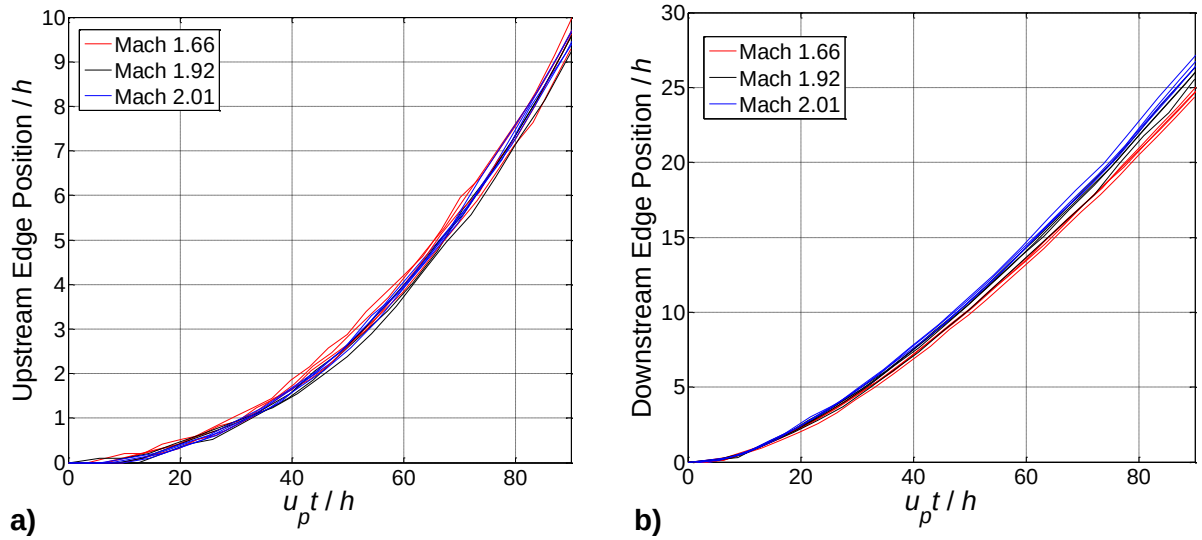

Fig. 21: Normalized particle field edge trajectories: a) upstream edge, and b) downstream edge.

there does appear to be some separation forming between the three Mach numbers at later times, the overall agreement between trajectories is good.

Figure 22 compares pressure traces of baseline shocks to those transmitted through the particle curtain far downstream of the interaction at x = 425 mm. The figure compares three baseline tests to three tests with a particle curtain. In order to assess the disturbance created by the ceiling and floor slits, the baseline tests were conducted with the particle curtain test section hardware installed. For each test the incident Mach number (measured upstream of x = 0) was about 1.66. The zero of the time axis corresponds to the time at which the incident shock crosses the trigger sensor seen in Fig. 1. Comparing the three baseline tests to one another, there are differences in shock crossing times owing to facility jitter, but the pressure traces are repeatable. The same observations hold true when comparing the three pressure traces of transmitted shocks. Jitter aside, because of the attenuation associated with the particle curtain, the three transmitted shocks arrive at a later time than the three baseline shocks. The pressure ratio of the baseline shocks is about 2.92, which gives a shock Mach number of 1.63 at the far downstream location. The shock Mach number is about 0.04 lower than that measured upstream of x = 0 due to wall effects and the ceiling and floor slit disturbances. In comparison, the pressure ratio of the transmitted shocks is about 2.45, which gives a shock Mach number of 1.50. To check forplanarity of the transmitted shock, tests were conducted where there was a sensor in the center of each of the four test section walls at x = 0.425 m. The tests showed the transmitted shock to be planar to within 2 μs.

Transmitted shock Mach numbers were calculated based on the time spent between the sensor at x = 425 mm, and an end wall sensor at x = 628 mm. In Table 3, the mean Mach number of the transmitted shock in the case without a curtain M_{sd} is compared to that measured during an interaction M_{td} for each incident shock Mach number. Using the mean shock Mach numbers and one-dimensional wave theory, the momentum and energy fluxes in the shock-induced flows with and without an interaction are compared in Table 3. For the three incident shock Mach numbers tested, the momentum and energy fluxes in the induced flow far downstream of the interaction are about 30 to 40% lower than those without a curtain.

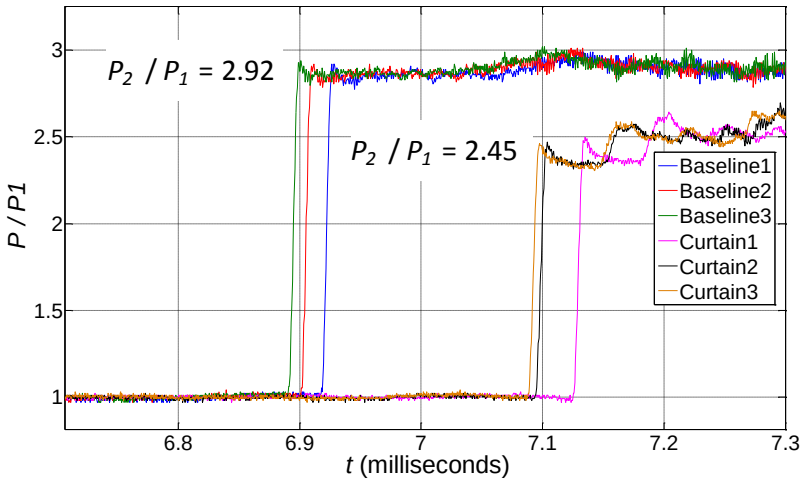

Fig. 22: Comparisons at x = 425 mm of pressures across three baseline shocks and three shocks that have been transmitted through a 2.2 mm thick curtain. In all cases the incident shock M_s is about 1.66 upstream of x = 0.

M_s	M_{sd}	M_{td}	*Momentum Flux Difference*	*Energy Flux Difference*
1.66 ± 0.02	1.65 ± 0.03	1.53 ± 0.04	-36 %	-31 %
1.92 ± 0.02	1.89 ± 0.03	1.74 ± 0.03	-34 %	-31 %
2.02 ± 0.02	1.99 ± 0.04	1.84 ± 0.02	-31%	-29 %

Table 3: Momentum and energy flux differences in the shock-induced flow far downstream.

4. Single Particle / Shock Interactions

4.1. Motivation

Once the current project developed, it became apparent that even the drag of a single spherical particle in unsteady compressible flow is not known as confidently as had appeared to be the case at the start of the program. A deeper knowledge of the historical literature on the subject suggested that considerable uncertainty remains and in fact some conclusions about the nature of shock/particle interactions may have been misguided. Therefore, this recognition motivated additional experiments on the drag of a single particle in a shock-induced flow. Such results are relevant to energetic material simulation just as are the dense gas-solid flows, since some stages of blast simulation involve more sparsely dispersed particles, and because even denser particle concentrations may be regarded as integrations of numerous individual particle response and particle-particle interactions. A small amount of additional funding was provided in the second year of the project to address this added deliverable.

4.2. Historical Background

Shock-particle interactions are fundamental in a multitude of engineering problems, but uncertainties in the unsteady particle response behind the shock wave hinder the ability to model and predict such flows. The most fundamental parameter that must be understood is the particle drag coefficient C_D. A variety of researchers over several decades have measured and correlated C_D in wind tunnels, ballistics ranges, and shock tubes; some of these experiments are reviewed by Igra and Ben-Dor [20] and Igra and Takayama [21]. In most practical situations, the dependence of the drag coefficient reduces to only two parameters, the particle Reynolds number based on the velocity difference:

$$Re_p = \rho_2 |u_2 - u_p| d_p / \mu_2 \tag{1}$$

and the particle Mach number based on the velocity difference:

$$M_p = |u_2 - u_p| / a_2 \tag{2}$$

where ρ_2, u_2, μ_2, and a_2 are the density, velocity, viscosity, and speed of sound in the gas behind the shock wave, respectively; u_p is the particle velocity; and d_p is the particle diameter.

A correlation describing C_D as a function of Re_p and M_p (or only Re_p for incompressible cases) has become known as the "standard drag curve" when it applies to steady flows, although several such "standards" exist. The most famous probably is that compiled in Hoerner [22], which also is found in numerous fluid dynamics textbooks. Henderson's correlation [23] is widely cited as well. Another useful example is the piecewise curve fit for incompressible conditions by Clift, Grace, and Weber [24] (reproduced in Ref. [20]), which covers an enormous range of Reynolds numbers; because it can be cumbersome to use, the single equation of Clift and Gauvin [25] (reproduced in Ref. [26]) is a close replacement for reasonable Reynolds numbers. Loth [26] modified this latter equation to account for compressibility, and Parmar et al [27] took a different approach to add compressibility through a new piecewise curve. The point at which compressibility becomes significant varies somewhat between authors, but is often agreed upon to lie somewhere between $M_p \approx 0.3$ and $M_p \approx 0.6$.

Though some differences exist in the predicted values of C_D returned by these various standard drag curves, they all are intended for use in a steady flow. When applied to unsteady flows, apparent

discrepancies arise. A number of studies have measured higher values of C_D for an unsteady flow than would be predicted by a standard drag model [21, 28-31]. In such cases, unsteadiness refers to the acceleration of a particle at rest when subjected to the flow behind a shock wave, or the deceleration of a particle in a ballistic test. These unsteady effects continue to occur long after passage of the shock wave over the particle, which produces an additional effect. A transient spike in drag is known to occur as the shock passes over a sphere, but lasts only for microseconds for particle sizes typical in shock tube and ballistics tests [32-34]. In most experiments, therefore, this transient drag rise is immeasurable and does not contribute to the particle motion when measurements commence subsequent to the immediate shock passage.

Unfortunately, in many experiments, it has proven difficult to separate unsteady effects from other influences upon the drag; for example, some early experiments that showed elevated C_D concluded that the cause was not due to unsteadiness, but rather, likely due to particle roughness or asymmetry or some other indeterminate effect [35-37]. Scatter in the data of individual experiments also clouds the results. Nonetheless, Igra and Takayama [21] were able to conclude that the particle C_D in their shock tube experiment significantly exceeded standard drag predictions over a wide range of Reynolds numbers. From their data, they produced a new correlation to represent unsteady values of C_D. Jourdan et al [31] later revisited these experiments and produced a new data set with some improvements in the experimental methodology. Although they generated a different correlation for C_D, they arrived at the same conclusion that C_D remained elevated over an equivalent unsteady value. Suzuki et al [30] supported these findings using a particle-injection method that significantly reduced the scatter of their data compared to previous efforts.

The point at which unsteady effects become significant can be defined by the acceleration parameter A_c:

$$A_c = \frac{d u_p}{dt} d_p / \left(u_2 - u_p\right)^2 \tag{3}$$

using the same terms as previously [21, 35, 36]. Unsteady effects are considered negligible if $A_c \ll 1$ (Refs. [21, 35]), which in practice corresponds to roughly $A_c < 0.1$ according to Igra and Takayama [21] or $A_c < 0.01$ according to Crowe et al [35]. The liquid phase study of Karanfilian and Kotas [38] suggests that the drag coefficient increase for $A_c = 0.01$ would be about 1% and for $A_c = 0.1$ it would be about 10%. Therefore, if A_c is small for an experiment, a standard drag model would be expected to predict the results – or, conversely, an elevated value of C_D would be attributable to some explanation other than unsteadiness.

With this consideration in mind, the shock tube studies of Igra and Takayama [21], Suzuki et al [30], and Jourdan et al [31] were re-examined. All the data for which the flow conditions could be determined are shown in Fig. 23, along with the standard drag prediction of Clift and Gauvin [25]. Despite the considerable degree of scatter in the data, it is evident that the values of C_D generally lie above the standard drag curve. However, this is not necessarily a result of the particle acceleration behind the shock wave in comparison to the steady flow inherent in the standard drag curve. Igra and Takayama demonstrate that for all of their data, $A_c < 0.1$; Jourdan et al state that $A_c < 0.035$; and an estimate of Suzuki et al's experiment yields $A_c < 0.01$ for all cases. Therefore, the effects of unsteadiness on C_D are expected to be small, suggesting that the elevated values of C_D detected in these experiments have some other source.

A possible explanation lies in the compressibility of the flow. At the time the cited experiments were conducted, the only known standard drag prediction to include compressibility was that of Henderson [23], which predicted a minimal effect (about 3%) for even the largest M_p in the data reproduced in Fig. 23. Based on this, the authors of the studies comprising Fig. 23 felt justified in neglecting the compressibility of their flow despite M_p as high as 0.85. Recently, both Loth [26] and Parmar et al [27] have produced new standard drag models that predict significantly higher effects due to compressibility. To examine whether compressibility may explain the elevated C_D in Fig. 23,

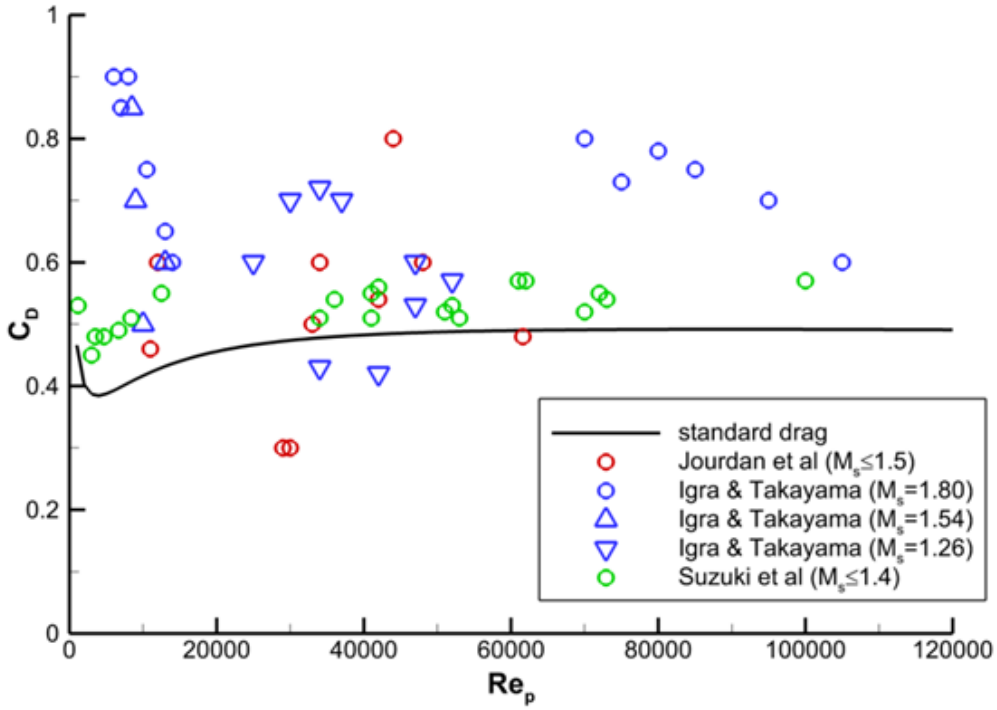

Fig. 23: Particle drag coefficients reproduced from Refs. [21, 30, 31] compared to the standard drag prediction of Ref. [25].

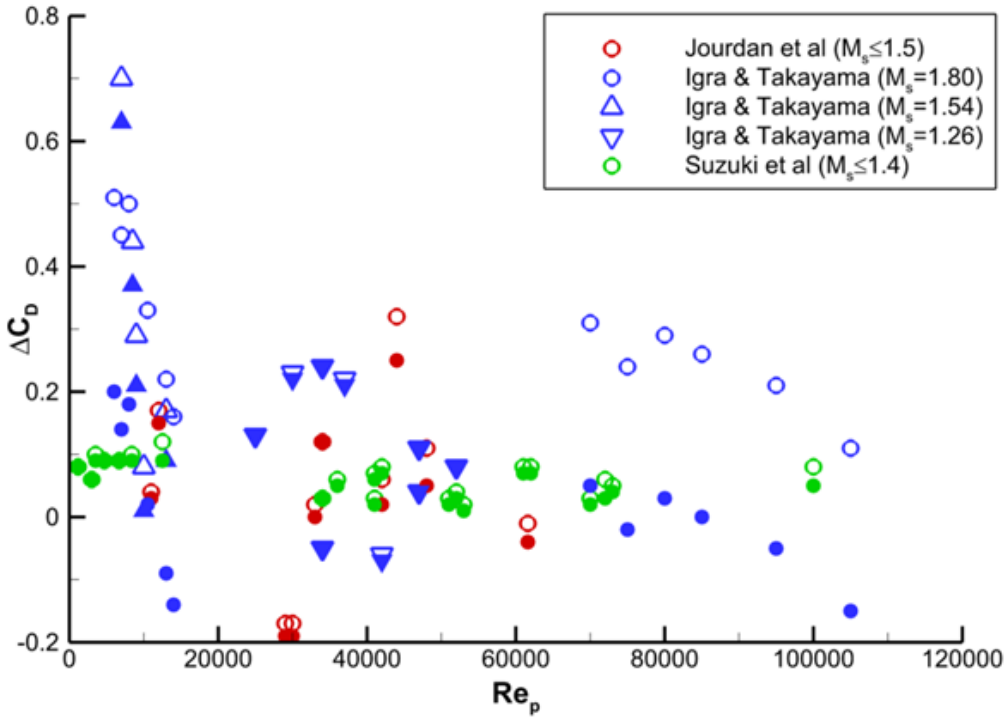

Fig. 24: Difference in measured particle drag coefficients [21, 30, 31] from the standard drag model of Clift and Gauvin [25] (hollow symbols) and the compressible drag model of Loth [26] (filled symbols).

the data were replotted in Fig. 24 as the difference between the measured values of C_D and two different standard drag models, one incompressible and one compressible. As can be seen, many of the data points shift closer to zero when compared with Loth's compressible model rather than Clift and Gauvin's incompressible model, indicating less discrepancy between the measured data and the prediction. The data points for relatively low shock Mach numbers M_s typically show minimal alteration when the compressible model is used, but the data for the largest Mach number display a considerably reduced discrepancy. This suggests that inclusion of compressibility into the standard drag model can more accurately predict the drag coefficient, and can explain the elevated C_D values seen in Fig. 23 without consideration of unsteady effects, consistent with the low values of A_c. Similar results were obtained comparing with Parmar et al's model rather than Loth's. The deviation in Igra and Takayama's data below Re_p of 10000 probably has a different explanation, as these used particularly lightweight foam particles.

Although reassessing past data with recent compressible drag predictions suggests that compressibility explains the drag increase, this is difficult to state conclusively given the significant scatter in the data and some uncertainty in the flow conditions and particle characteristics. New experiments are necessary to establish that the elevated values of C_D can be explained by compressibility rather than unsteadiness, which has motivated the present shock tube study.

4.3. Shock Tube Modifications

A schematic of the multiphase shock tube as modified to test the acceleration of spheres in shock-induced flows is shown in Fig. 25. Only the downstream portion of the driven section is visible, showing the single-particle drive system used to insert spheres into the shock tube test section. Prior to a test, about 500 individual 1 mm stainless steel spheres having a density of 7612 kg/m^3 are loaded into a sphere holder tube having a diameter of 1.1 mm. Since the uncertainty in the time of diaphragm burst is about 5 seconds, many spheres can be dropped to ensure that one will be present in the test section upon arrival of the incident shock. The spheres are manufactured by CCR Products, and according to the manufacturer have diameter and sphericity tolerances of 0.0003, and 0.0002 mm, respectively. The drive system attaches to a mounting plate that is bolted to the top of the shock tube. The angle of the top of the mounting plate is 0.5-degrees with respect to the horizontal to prevent the spheres from rolling into the test section prematurely. A precision Aerotech linear motor (Pro165LM) drives a 0.90 mm push rod into the sphere holder tube. To prevent buckling of the thin push rod, rod

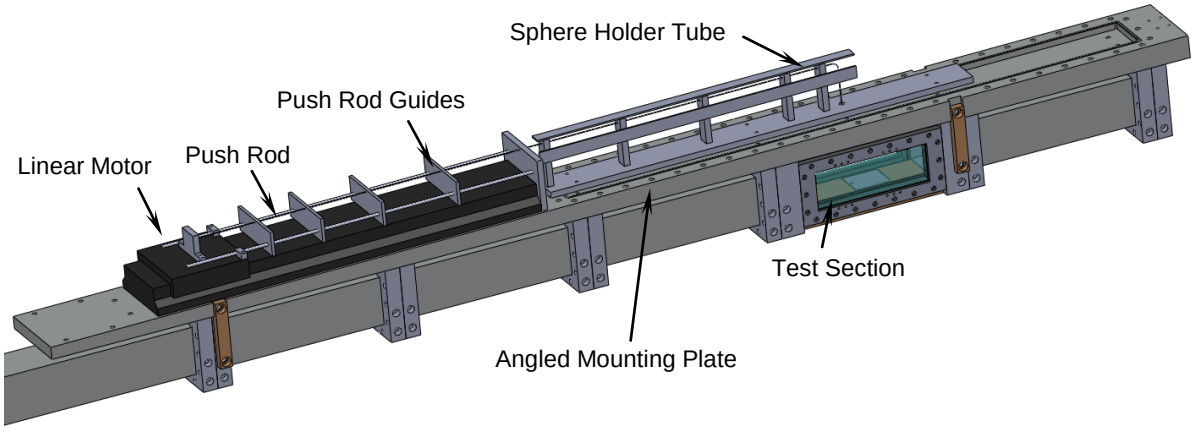

Fig. 25: Schematic of the downstream end of the driven section of the multiphase shock-tube, modified with the single-particle apparatus.

guides are also driven by the motor along two shafts. The motor is controlled with a PC and an in-house developed LabVIEW (National Instruments) code. The spheres fall out of the tube through a 1.1 mm hole in the test section ceiling. The spheres that fall through the test section prior to arrival of the incident shock travel exit through a 6 mm hole in the floor into a 6 mm collector tube. The number of spheres present in the test section can be controlled by varying the speed of the motor. To obtain the drag of single spheres the motor is typically run at speeds of 25-75 mm/s. Since the shock and post-shock velocities are much higher than those of the particle prior to shock, the particle is essentially 'frozen' with respect to the incident shock and its downward motion is negligible.

The same PCB pressure sensors as used previously also were employed for the single-particle tests. As before, a sensor about 0.5 m downstream of the diaphragm is used to trigger the data acquisition systems. In the experiments described in this section of the report, $x = 0$ corresponds to the initial sphere location at $t = 0$, which is the arrival time of the incident shock. Four sensors are placed near $x = 0$ to characterize the incident shock and its induced flow during a test. One sensor is mounted in the ceiling at about $x = 64$ mm and three sensors are placed at $x = 10$, 41, and 64 mm along the shock tube floor.

The high-speed schlieren imaging system was modified to suit the needs of the single-particle experiments. The same light source as used previously was continued for these experiments, but the high-speed camera was configured differently. Two fields of view were used with the first having dimensions of about 46×19 mm^2 and the second 46×38 mm^2. The larger field of view was chosen in instances to increase the likelihood for a particle to be present in the field of view upon arrival of the incident shock and the smaller field of view was chosen to have an increased framing rate. For the smaller field-of-view the framing rate was 100 kHz, and the image resolution was 304×128 pixels. For the larger field-of-view the framing rate was 51 kHz, and the image resolution was 304×256 pixels. The exposure time for both fields-of-view was 1 μs. Each image was saved in 8-bit format.

4.4. Results of Particle Tracking Velocimetry

The sphere drag coefficients are based on velocities obtained from particle tracking velocimetry data, which were generated using high-speed schlieren images. An example of such a sequence of schlieren images acquired during a Mach 1.68 test at a framing rate of 100 kHz is shown in Fig. 26. Three particles appear in the sequence. As will be discussed, particle-particle interactions in this particular test were not significant enough to cause a measurable difference in drag coefficient between the three spheres. In each schlieren image, the particles appear in shadow with a diameter of about 6 pixels. In Fig. 26a, at t = 5 μs, the incident shock has passed over the particles. Reflected bow shocks appear, which are a transient effect since the particle Mach number at the time is about 0.75. With continuing time the bow shocks propagate upstream until they are no longer present in the field of view. From $t = 5 - 2005$ μs, the three particles propagate downstream through the field of view.

Using the particle shadows during propagation, the particle velocity was computed using the PTV algorithm implemented in the software package in Davis 7.4. Prior to PTV processing, each raw image was inverted using a threshold of about 80 counts. The inverted images were then processed with PTV using validation filters to limit the particle velocities and accelerations to reasonable values that were dependent on the flow conditions. The PTV data for the lower-most sphere of Fig. 26 are given in Fig. 27. Raw PTV data are shown in Fig. 27a and the data smoothed with a nine-point centralized (90 μs) moving average filter are given in Fig. 27b. From Fig. 27a, the apparent noise in the PTV data is about 1-3 m/s, which corresponds to about 0.1-0.2 pixels of particle displacement. For about the first 0.1-0.2 ms of particle travel, the displacements were small enough (less than about 0.1-0.2 pixels,) to therefore be within the noise band and to render the PTV data unreliable. Thus, these early time data points are not included in the drag coefficient calculations. The PTV data for the higher two nominal shock Mach numbers exhibited similar characteristics to that in Fig. 27, except with higher velocity magnitudes and accelerations.

The sphere drag coefficient was determined by fitting the particle velocities to the drag relation. The drag relation for an accelerating sphere in a constant velocity fluid is [21]:

$$C_D = \frac{4\rho_p d_p \frac{\partial u_p}{\partial t}}{3\rho_2 (u_2 - u_p)^2} \tag{4}$$

Solving the drag equation for u_p yields:

$$u_p = u_2 - \frac{u_2}{u_2 A t + 1} \tag{5}$$

where

$$A = \frac{3\rho_2 C_D}{4\rho_p D_p} \tag{6}$$

Then by least squares regression, Eq. (5) is fit to the velocity data to determine the one unknown parameter, C_D. As indicated by Eq. (5) and Eq. (6), an accurate measurement of C_D requires

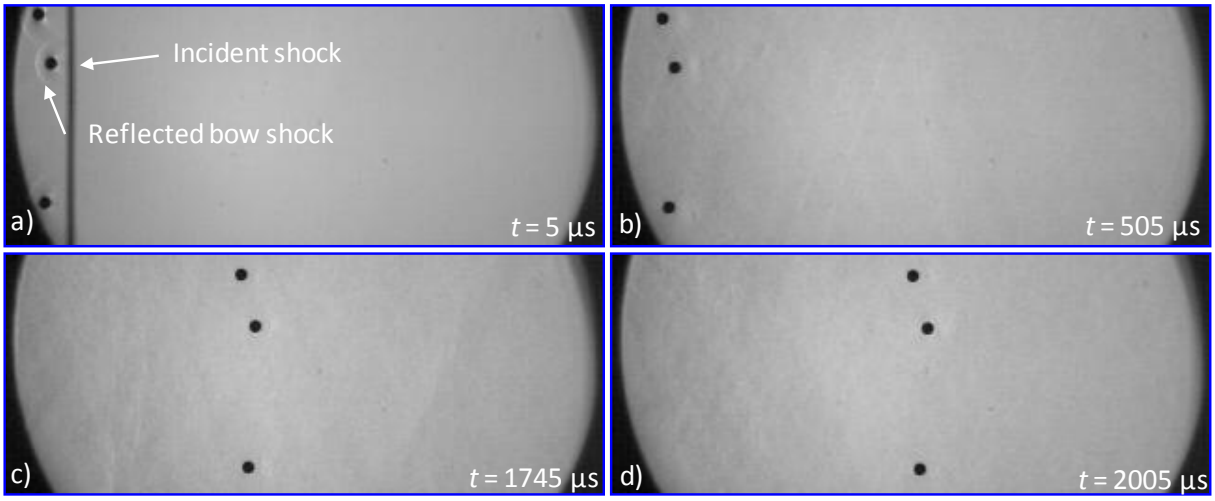

Fig. 26: Sample schlieren images for a Mach 1.68 test with three particles within the field-of-view at times: a) t = 5 μs, b) t = 505 μs, c) t = 1745 μs, and d) t = 2005 μs.

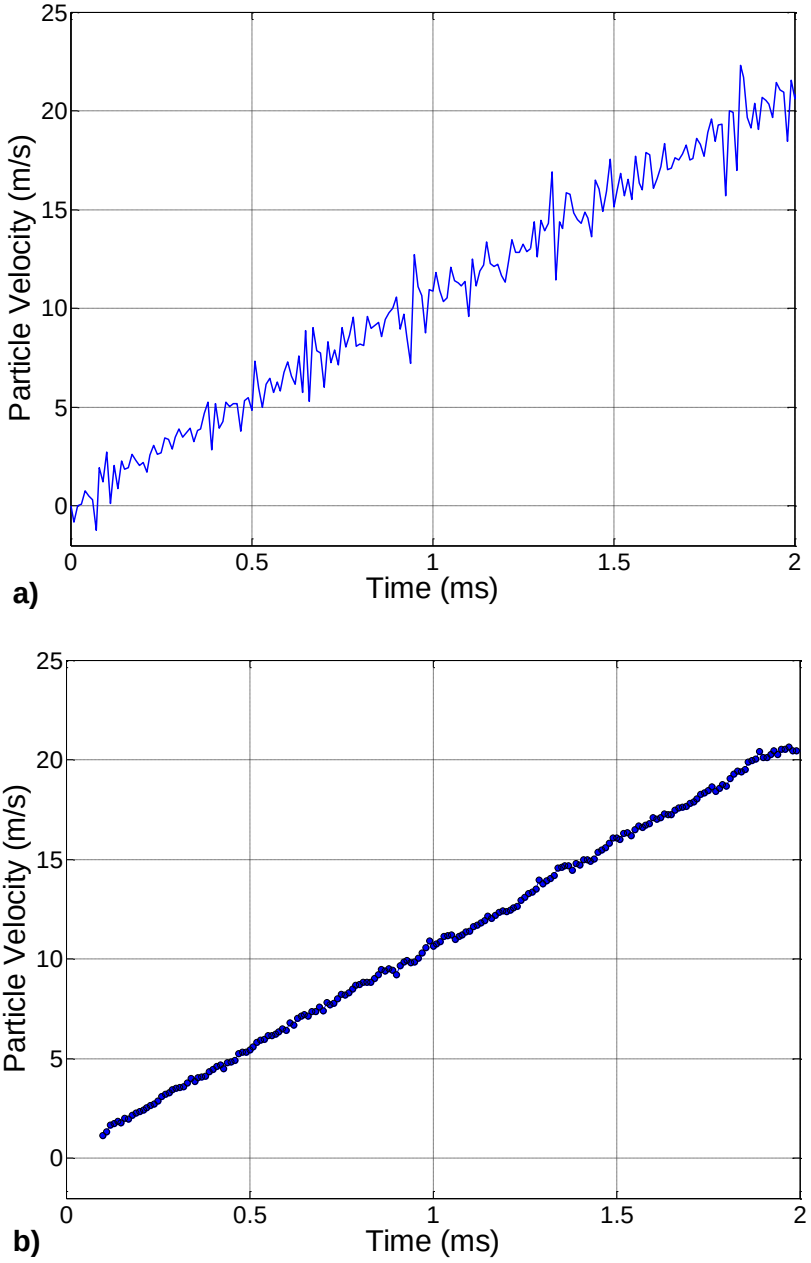

Fig. 27: Particle tracking velocimetry results from the lower-most particle of Fig. 26: a) raw PTV data, and b) 9-point (90 μs) smoothed PTV data.

knowledge of the fluid properties around the immersed sphere. In the case of the present data, it is assumed that the flow properties remain constant during the times where C_D is computed. Pressure traces in the vicinity of the sphere were used to assess the validity of this assumption. An example trace is shown in Fig. 28. Following the pressure increase caused by the incident shock, the pressure is relatively constant. While it is difficult to discern small changes in flow velocity and density from such a pressure trace, the relatively constant pressure indicates that large flow variances do not occur over the 2 ms test time.

In Fig. 29, least squares fits of the particle velocity predicted by Eq. (5) are compared to the PTV data of Fig. 27b. Over the 2 ms data acquisition time Re_p decreases from about 25,000 to 23,000, while M_p changes from about 0.75 to 0.7. The correlation of Parmar et al. [27] suggests that C_D should decrease by about 6% over this 2 ms. To evaluate if such a change could be detected in the data, a piecewise fit of Eq. (5) was applied where the segment length was 0.5 ms. The method gave drag coefficients of 0.55, 0.54, 0.54, and 0.55 for the times of 0-0.5, 0.5-1.0, 1.0-1.5, and 1.5-2 ms, respectively. The piecewise fit is shown in Fig. 29. The fact that C_D varies so little without a clear trend over the data acquisition period suggests that the piecewise method for measuring C_D is unable to resolve any small changes that may be occurring over the rather limited range of flow conditions range tested. In comparison, a constant C_D = 0.55 fit to the data is also shown in Fig. 29. Since a discernable difference was not obtained using the piecewise method, the constant C_D method is used herein.

The top two particles seen in Fig. 26 were also measured to have C_D = 0.55. This suggests that the in-plane spacing (note that the spanwise spacing is not known) of the top two particles was great enough to preclude particle-particle interactions that could cause a significant change in drag. Although, as is discussed below, this was not found to be the case for measurements made for the two higher shock Mach numbers.

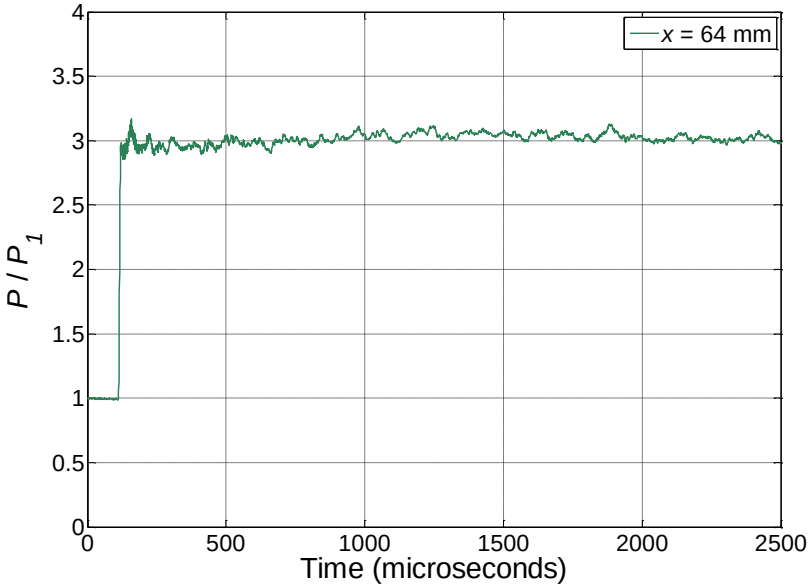

Fig. 28: Ceiling pressure during the M_s = 1.68 test of Fig. 26 and Fig. 27.

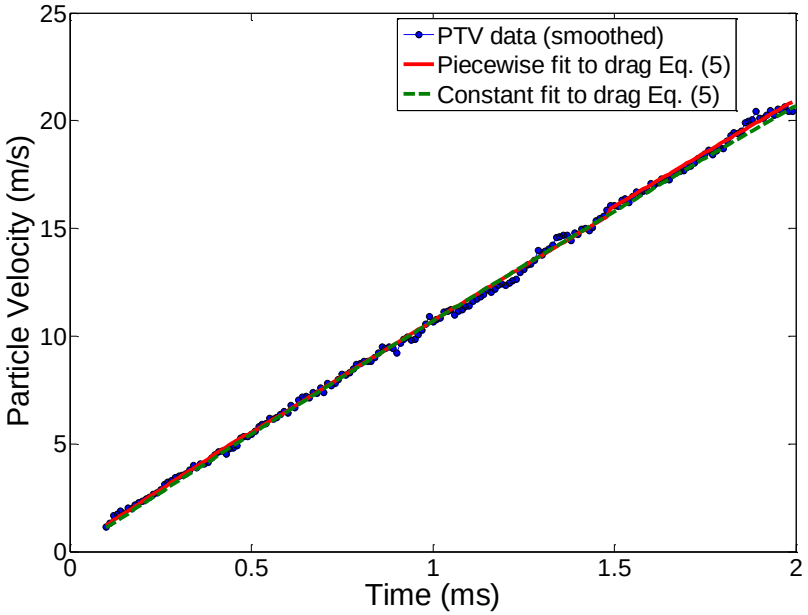

Fig. 29: Particle tracking velocimetry data and fits based on drag relation Eq (5).

4.5. Discussion of Single-Particle Drag

A sequence of images acquired during a M_s = 2.05 test is depicted in Fig. 30. Note that the images have been cropped. The initial particle Mach number is about 1. In comparison to the lower Mach number test of Fig. 26 where M_2 = 0.75, the effects of compressibility are naturally much more pronounced and recompression shocks are observed in the particle's wake. The extent of the recompression shocks is seen to increase in the images from t = 19 through 58 μs. A greater particle Mach number also significantly increases the drag coefficient. For example, using the method described above, C_D was measured to be 0.83, or about 50% greater than the case of Fig. 26.

Increasing the particle Mach number from about 0.75 through 1 was also observed to significantly increase the distance for which particles interact. This result is not surprising when considering the nearly normal waves that occur in a near sonic flow around a sphere. Examples of such interactions are shown in the sequence of Fig. 31. Upstream propagating reflected bow shocks are observed in the images from t = 6 through 45 μs. Also, over these times and similar to the single sphere sequence in Fig. 30, the recompression shocks grow in size. Eventually the recompressions interact as is evident in Fig. 31d. The drag coefficient for the bottom most sphere in Fig. 31 is measured to be 0.94, which will be shown to be well outside of the scatter for measurements of single spheres in similar flows. Again, the spanwise separation of the spheres was not measured so it is difficult to currently determine exactly how the sphere separation modifies the drag. What can be concluded is that it is necessary to omit data for which particle-particle interactions occur, or the drag coefficients may be found artificially high with a greater degree of scatter.

With the above considerations in mind, extra care was taken at the two higher Mach numbers to only include sphere trajectories for which particle-particle interactions were not present. The results at all three nominal test conditions are summarized in Table 4. For each test, the conditions in the shock-induced flow computed from normal shock theory are given. Also noted is the time for which the particle was tracked Δt to determine its drag and the corresponding particle Mach and Reynolds number ranges during this time. The acceleration parameter, computed from the measured C_D and

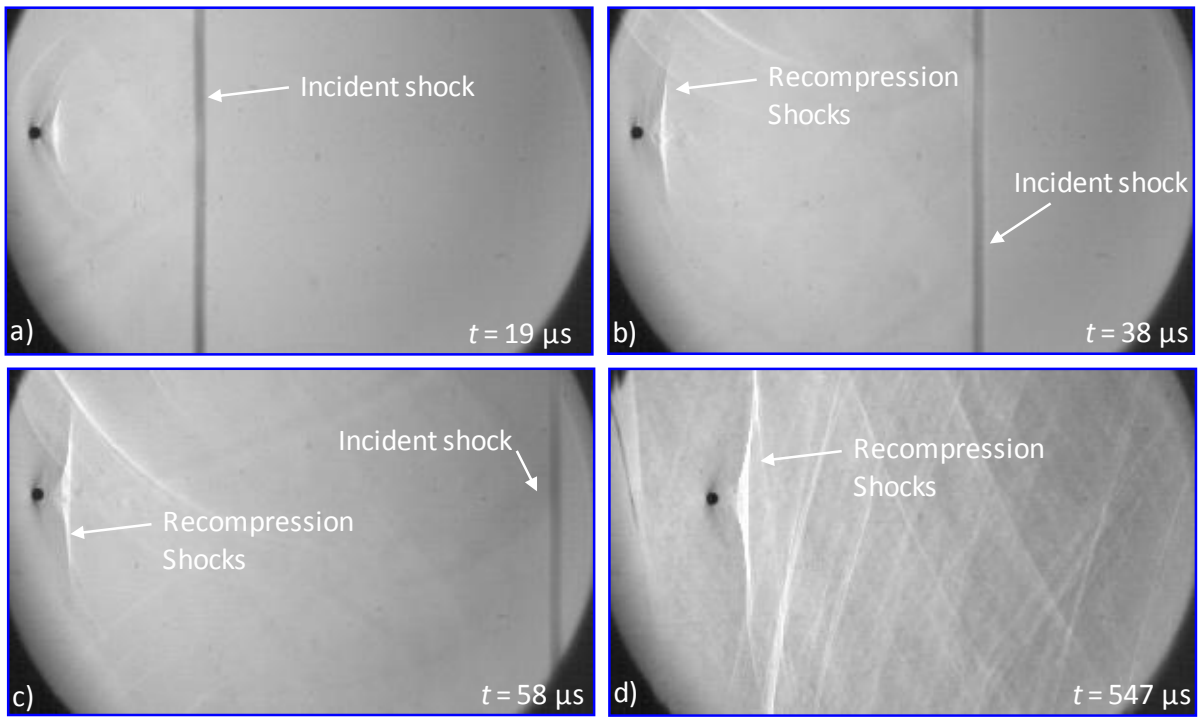

Fig. 30: Schlieren images for a Mach 2.05 test at times: a) *t* = 19 µs, b) *t* = 38 µs, c) *t* = 58 µs, and d) *t* = 547 µs.

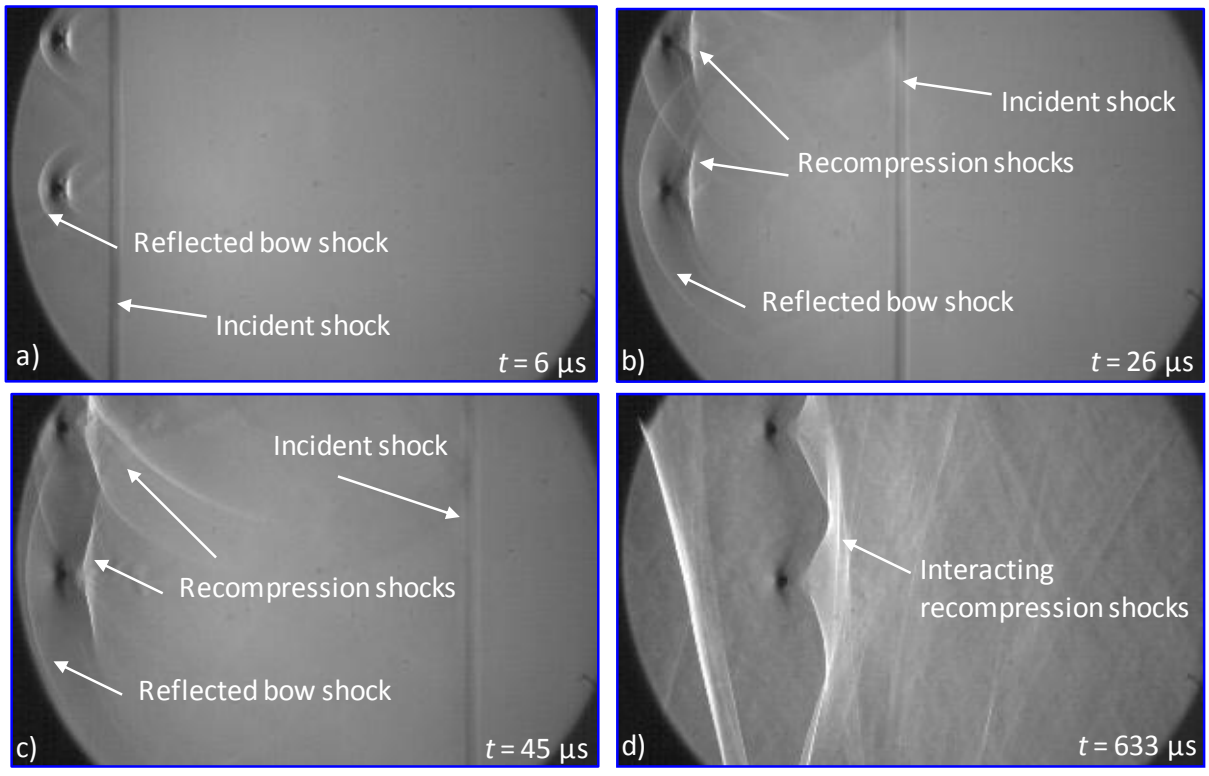

Fig. 31: Schlieren images showing two interacting spheres during a Mach 2.02 test at times: a) *t* = 6 µs, b) *t* = 26 µs, c) *t* = 45 µs, and d) *t* = 547 µs.

Run #	M_s	M_2	T_2, K	ρ_2, kg/m^3	U_2, m/s	Δt (ms)	M_p (range)	Re_p (range)	A_c	C_D
121a	1.68	0.75	428	2.12	312	0.1-2.0	0.75-0.70	27000-25300	0.0001	0.55
121b	1.68	0.75	428	2.12	312	0.1-2.0	0.75-0.70	27000-25300	0.0001	0.55
121c	1.68	0.75	428	2.12	312	0.1-2.0	0.75-0.70	27000-25300	0.0001	0.55
128	1.67	0.74	425	2.11	307	0.1-2.0	0.74-0.70	26600-25000	0.0001	0.52
129	1.68	0.76	428	2.14	314	0.1-2.0	0.75-0.70	27400-25600	0.0001	0.55
135	1.94	0.92	485	2.52	408	0.1-1.2	0.92-0.85	38400-35400	0.0002	0.73
136	1.93	0.92	485	2.52	407	0.1-1.2	0.92-0.85	38400-35500	0.0002	0.71
145a	1.92	0.91	481	2.50	402	0.2-1.2	0.90-0.84	37300-34600	0.0002	0.76
145b	1.92	0.91	481	2.52	402	0.2-1.2	0.90-0.84	37400-34700	0.0002	0.75
150	1.93	0.91	487	2.52	404	0.2-1.2	0.90-0.84	37400-34700	0.0002	0.72
167	2.05	0.99	511	2.68	447	0.1-0.8	0.99-0.91	43300-40000	0.0002	0.83
172	2.05	0.99	511	2.69	449	0.1-0.7	0.99-0.92	43600-40600	0.0002	0.82
174	2.05	0.99	512	2.67	448	0.1-0.8	0.99-0.91	43200-39800	0.0002	0.83
175	2.04	0.99	512	2.67	447	0.1-1.0	0.99-0.88	43100-38700	0.0002	0.84

Table 4: Shock Tube Experimental Conditions for a 1mm sphere having a density of 7612 kg/m^3.

Eqs. (3) and (4) is also given. In all cases $Ac < 0.0003$. Therefore, flow unsteadiness is not expected to play a noticeable role in increasing the particle drag [21, 35]. On the other hand, it is evident from Table 4 that as flow compressibility increases with M_p, so does C_D. In summary for the three nominal M_2 values of 0.75, 0.92, and 0.99, the mean C_D computes to 0.54 ± 0.03, 0.74 ± 0.06, and 0.83 ± 0.05. The uncertainty bands correspond to 95% confidence intervals based on student-t theory.

The data suggest that increased compressibility is the cause of the increased sphere drag and not flow unsteadiness. It is also useful to compare the current measurements to correlations that include Mach number such as the classic relation of Henderson [4] and the two more recent forms given by Loth [26] and Parmar et al. [27]. Figure 32 shows such a comparison to the current $M_p = 0.99$ data. The data lie substantially above the Henderson [23] curve, which highlights how previous researchers such as Suzuki et al. [30] may have reached the conclusion that compressibility could not have explained their observed drag increase. However, a comparison of the current data to that of more recent correlations is highly suggestive that compressibility is in fact the cause.

The current data for all three Mach numbers are plotted with the correlations of Loth [26] and Parmar et al. [27] in Fig. 33. The measurements at a nominal M_2 of 0.75 agree quite well with the Parmar et al. correlation, while as M_2 increases, the current drag coefficients tend to fall closer to those predicted by Loth. Although it is not clear which correlation performs better, it is evident that compressibility, or Mach number of the induced flow, correlates well with the increased drag coefficients. The current results are therefore supportive of the argument that the increased drag coefficients of spheres having low acceleration parameters reported in previous shock tube studies [21, 28-31] can be attributed to compressibility rather than flow unsteadiness. Other factors may play a role as well in some experiments, such as freestream turbulence levels or particle roughness or asymmetry.

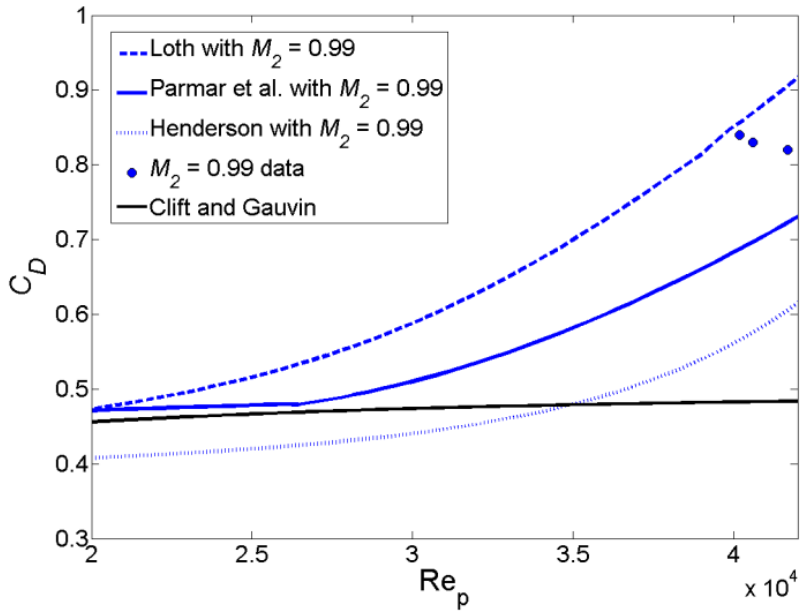

Fig. 32: Comparison of M_s = 2.05 (M_2 = 0.99) data to correlations of Loth [26], Parmar et al. [27], Henderson [23], and Clift and Gauvin [25]. The correlation curves were generated using the average initial conditions found in Table 1.

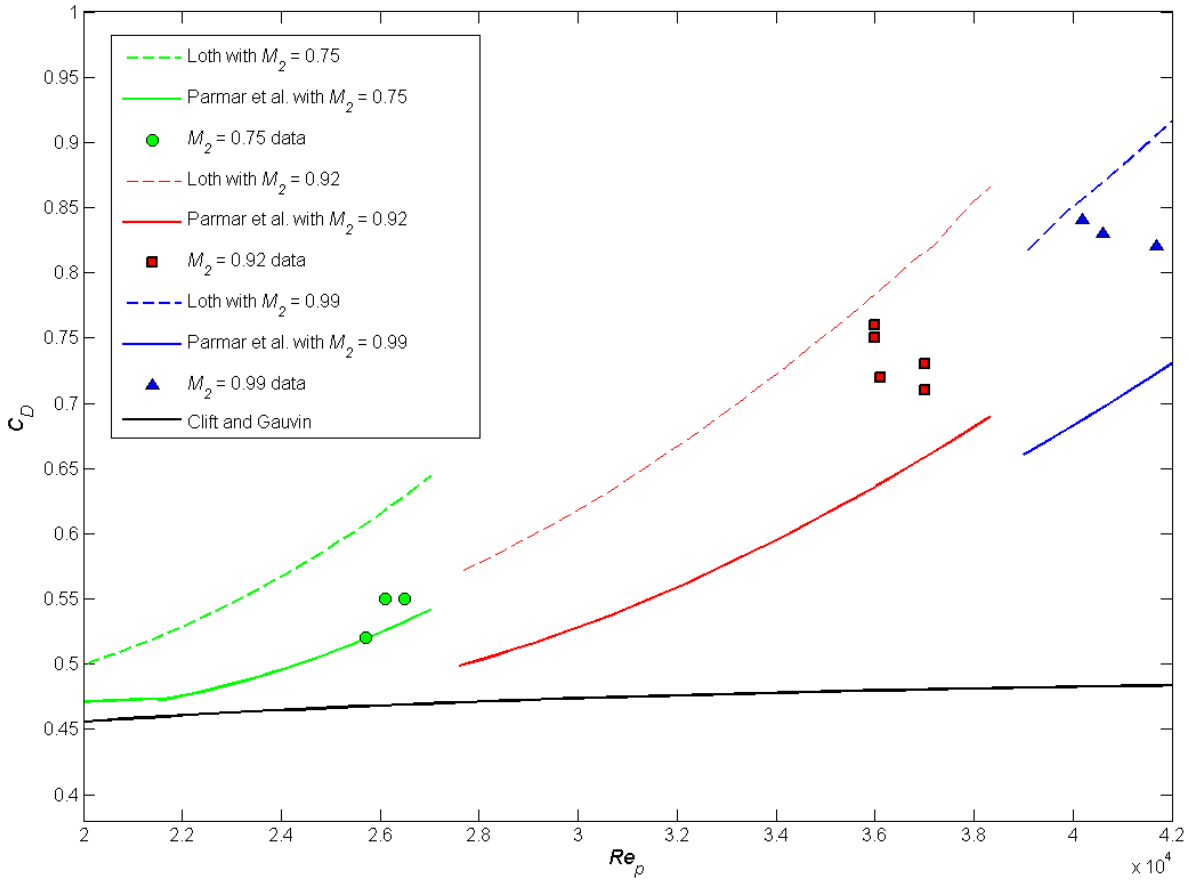

Fig. 33: Comparison of current data to correlations of Loth [26], Parmar et al. [27], and Clift and Gauvin [25]. The correlation curves were generated using the average M_2, computed from the average M_s and initial conditions found in Table 1.

5. X-Ray Diagnostics

5.1. The Flash X-Ray System

Chapter 5 focuses on the flash x-ray measurements made for shock interactions with dense particle fields. As discussed in Section 3.5, the high-speed schlieren imaging data provided valuable insight into the flow and particle behavior. However, it was not possible to make measurements within the particle field using visible light. To penetrate the optically-dense medium, X-ray measurement techniques previously utilized for multiphase flows and high-energy physics were adapted to the uncommon difficulties of the present problem. It was determined that the continuous x-ray sources used in previous low-speed studies [13, 14] could not provide adequate light in the microsecond timescales of interest. Alternatively, flash x-ray sources are able to provide intense beams that last tens of nanoseconds, essentially 'freezing' the flow in a similar fashion to laser diagnostic measurements in fluids experiments. The use of a flash x-ray imaging system is able to measure two important quantities: 1) by measuring the x-ray attenuation through the particle field, the particle volume fraction can be directly measured, and 2) using two flash x-ray sources separated in time, x-ray particle tracking velocimetry, or PTV, can provide particle velocities in the dense flow that is inaccessible to standard laser diagnostic techniques.

A photo of the 450 kV flash x-ray system is given in Fig. 34. The system has two channels of output, each having a characteristic photon energy of 450 keV, which corresponds to a wavelength of about 3 pm. Owing to bremsstrahlung (brems) radiation, the energy in the x-ray beam has a broad distribution with the intensity peak likely occurring at about one third the rated source wavelength, or at about 150 keV. Prior to firing a channel of the system, a Hewlett Packard Marx generator (model 43734-62900) is charged to a potential of 27-35 kV, (depending on the desired photon flux), with a L-3 high-voltage power supply (model 3147A). The system uses sulfur hexafluoride and nitrogen for dielectric purposes. Upon triggering, about 6 MA of current flows from the capacitor banks to the x-ray tube heads, resulting in an intense x-ray beam having a duration of tens of nanoseconds. It takes about 10 seconds to charge each Marx generator, so only one shot of each channel per shock tube test is possible.

At a distance of about 1m from the point source output, the energy in each incident beam is at a maximum of about 20 mR (i.e., when the capacitor banks are charged to 35 kV). Several options exist from the manufacturer for x-ray generating tubes. The tubes, which are placed in the remote tube heads labeled in Fig. 34 can be ordered with a spot size of 1-5 mm. The benefit of using a larger spot size is increased tube life, whereas the benefit of using a smaller spot size, as is detailed below, is

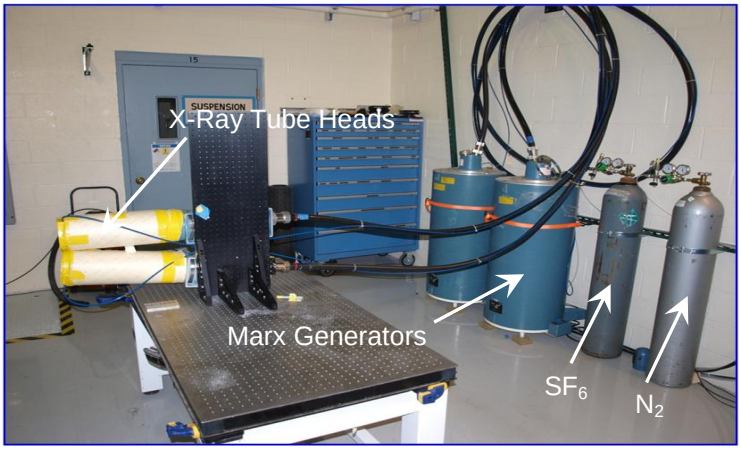

Fig. 34: Photo of the 450 kV flash x-ray system.

improved image quality. With the latter benefit in mind, the tube heads used for the current work had an effective spot size of about 1 mm. The tube heads lasted about 50 shots each.

A Rad-icon detector (RadEye2 EV) was used to image the incident x-rays. The sensor used a Gadolinium Oxide scintillator to convert x-ray photons to visible photons that were imaged by a CMOS sensor. The 12-bit sensor had 1k × 1k array of 100 micron pixels, yielding a sensor of about 4 inches in each dimension. Owing to readout limitations, the minimum delay between the triggering of the detector and image recording was about 150 ms. Since it takes roughly 10 ms for the incident shock to travel down the length of the shock tube, a shock could not be used to trigger the detector.

The experimental timing sequence was as follows. The detector was instructed to begin recording during the pressurization of the driver section. Although a shock wave could not be used to begin recording, it could be used to end recording, which resulted in detector integration times of about 2-4 seconds. It was desirable to minimize the sensor integration time to minimize detector noise. A ceiling sensor (PCB 113B27) at x_i = -68.6 mm was used to trigger the flash x-ray source. At M_s = 1.66, it takes the incident shock about 130 μs to reach the upstream edge of the curtain at x_i = 0. Using the pressure signal and a Stanford Research Systems delay generator (DG645) the particle field was imaged at interaction times t_i = 0-300 μs. The same sensor was also used to trigger the detector to end recording.

5.2. Image Processing

A standard flat-field correction process was applied to each test image. Prior to the acquisition of each image, an offset image was acquired without x-ray signal to account for variations in background intensity of the CMOS sensor. The offset varied from about 100-400 counts. To correct for variations in detector response to the x-rays, as well as true variations in the x-ray beam, a full-scale, or gain image was also acquired. The gain image was corrected by subtracting the offset image. Following an offset subtraction, the test images were then normalized by the corrected gain image resulting in a near flat-field image where particles were not present. An example of such an image showing the particle field at an interaction time of t_i = 268 μs is given in Fig. 35a. The image is 100 mm × 64 mm^2 and is located at the wall-normal center of the test section.

The streamwise intensity profile averaged over the middle 8 mm of the image in Fig. 35a is shown in Fig. 35b. Even with the flat-field correction described above there is a clear nearly linear decrease in intensity with increasing streamwise position in locations where no particles are present. This artifact is attributed to noise acquired during the three second integration time of the image. Although not repeatable, each image acquired in the study exhibited either a nearly linear or nearly quadratic pattern of changing intensity across the streamwise dimension of the image. Therefore, on an image-by-image basis, an additional correction using either a linear or quadratic fit was performed. As is demonstrated below, for all images presented herein, this additional correction successfully brought the intensity levels to a nearly constant value for pixels outside of the particle field location.

5.3. Particle Volume Fraction Measurements

A schematic of the setup used to measure the particle volume fraction during an interaction is shown in Fig. 36. Note that the schematic is in the plan-view (x-z) plane. Each sidewall of the test section was outfitted with an aluminum window having a length of 225 mm, a height of 64 mm, and a thickness of 10 mm. For the particle volume fraction measurements, one x-ray source that was vertically (y-axis) aligned with the test section wall normal center was used. The x-ray source to object (SOD) distance was 136 cm, where the object location is defined here to be at the spanwise center of the test section, or at z = 0. The detector (details above) was attached to the test section

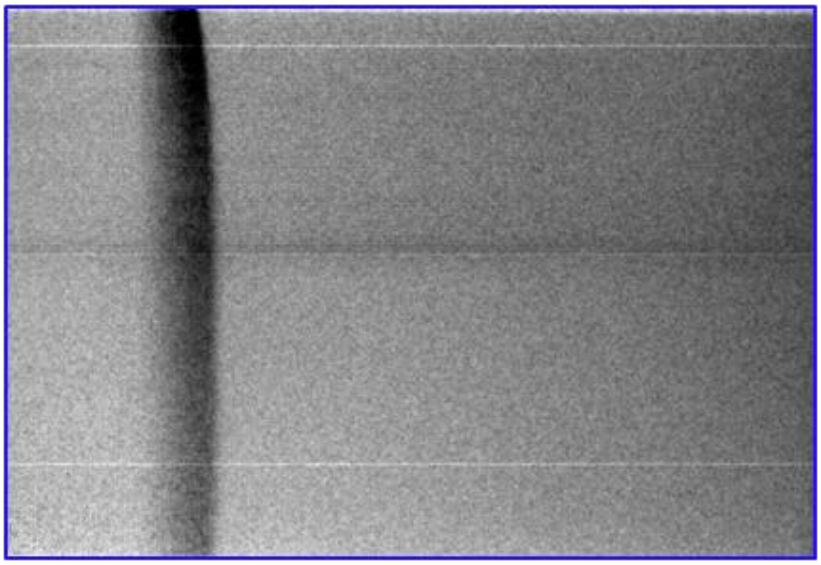

a)

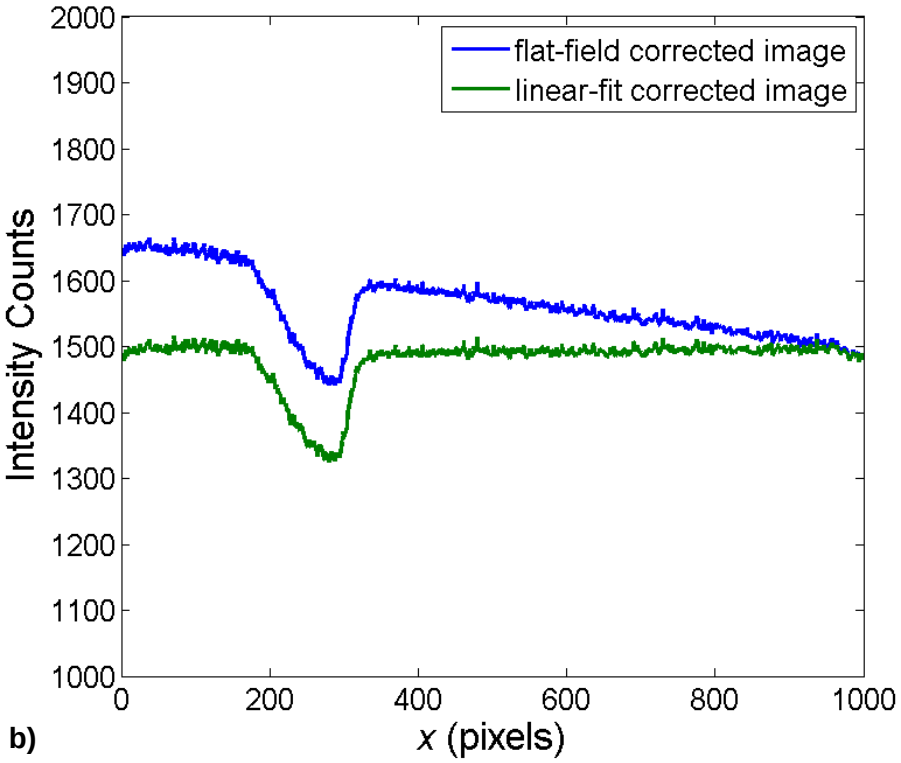

b)

Fig. 35: Particle field at t_i = 268 μs: a) image (100 × 64 mm^2) following a standard flat-field correction procedure showing the 8mm tall rectangle over which the streamwise intensities are averaged, and b) averaged streamwise intensity profile for the image and a linear-fit corrected profile.

sidewall at a distance (IOD) of about 8 cm from $z = 0$. The x-ray beam is a point source, which results in a geometric blur b [39]:

$$b = \frac{S \times OID}{SOD} \tag{7}$$

Since the particles span nearly the entire test section width, their blur will vary with spanwise location. With the experimental geometry of Fig. 36, the blur width for particles at the detector side of the test section (z = -4 cm) is about 30 microns. The blur increases to about 90 microns for particles at the source side of the test section (z = 4 cm).

The typical image field-of-view for the particle volume fraction measurements is given in Fig. 37. The image size was about 50 × 64 mm, which covered 500 × 640 pixels of the detector. The initial curtain location was in the upstream portion of the image to allow for recording during the downstream propagation of the particle field. As is shown in Fig. 36, this resulted in an angle between the streamwise center of the curtain and the centerline of the x-ray source θ of about 1.5-degrees. It is likely that this small angle is great enough to produce bias errors.

If an incident x-ray beam with intensity I_0 travels through a medium with density ρ and thickness w, the resulting intensity I is:

$$I/I_0 = e^{-A\rho w} \tag{8}$$

where A is the mass x-ray attenuation coefficient, which has been tabulated [40] for common materials. Thus if the attenuation coefficient and material properties of the medium are known, the total thickness of the medium can be computed.

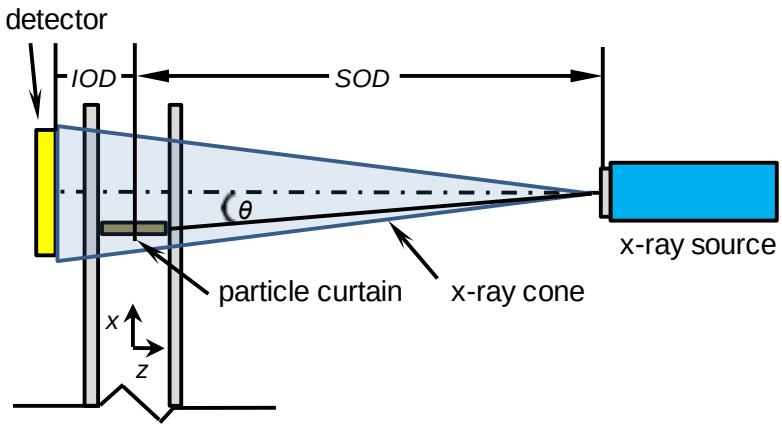

Fig. 36: Schematic of the single-source flash x-ray configuration used to measure the particle volume fraction during an interaction with a spanwise parallel curtain.

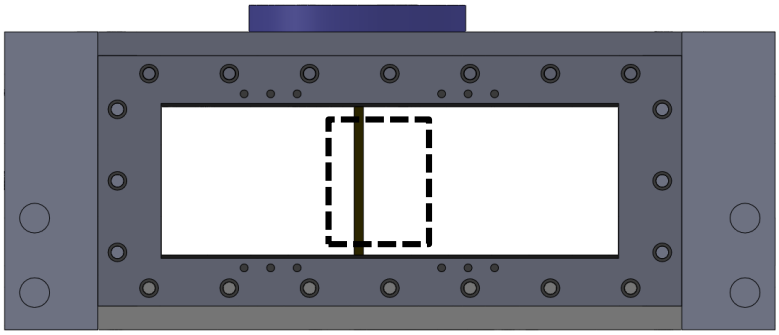

Fig. 37: X-ray imaging field-of-view for the particle concentration measurements.

A goal of the current work is to determine the particle volume fraction of the particle field following the impingement of the incident shock. Assuming a constant particle curtain spanwise width w_0, the volume fraction of the curtain through a given cross section is given by:

$$\varphi = {w_g}/{w_0} \tag{9}$$

where w_g is the total width of soda lime spheres through which the x-rays have traveled. Substituting w_g given from Eq. (9) into Eq. (8) and solving for φ yields:

$$\varphi = \frac{\ln\frac{I}{I_0}}{-Aw_0\rho_g} \tag{10}$$

where ρ_g is the density of the soda lime glass, which is 2.52 g/cm^3.

The mass x-ray attenuation coefficient A is a function of the initial incident intensity I_0. Rather than account for the broad photon energy distribution of the beam and the attenuation through the aluminum test section windows, a calibration method with a glass step-wedge was employed. The step-wedge consisted of fifteen glass microscope slides that were each 75 mm × 25.4 mm × 0.96 mm. The density of the glass slides was 2.4 g/cm^3. The slides were stacked such that incident x-rays passed through fifteen steps of increasing glass thickness. The step-wedge appears in the bottom of the image

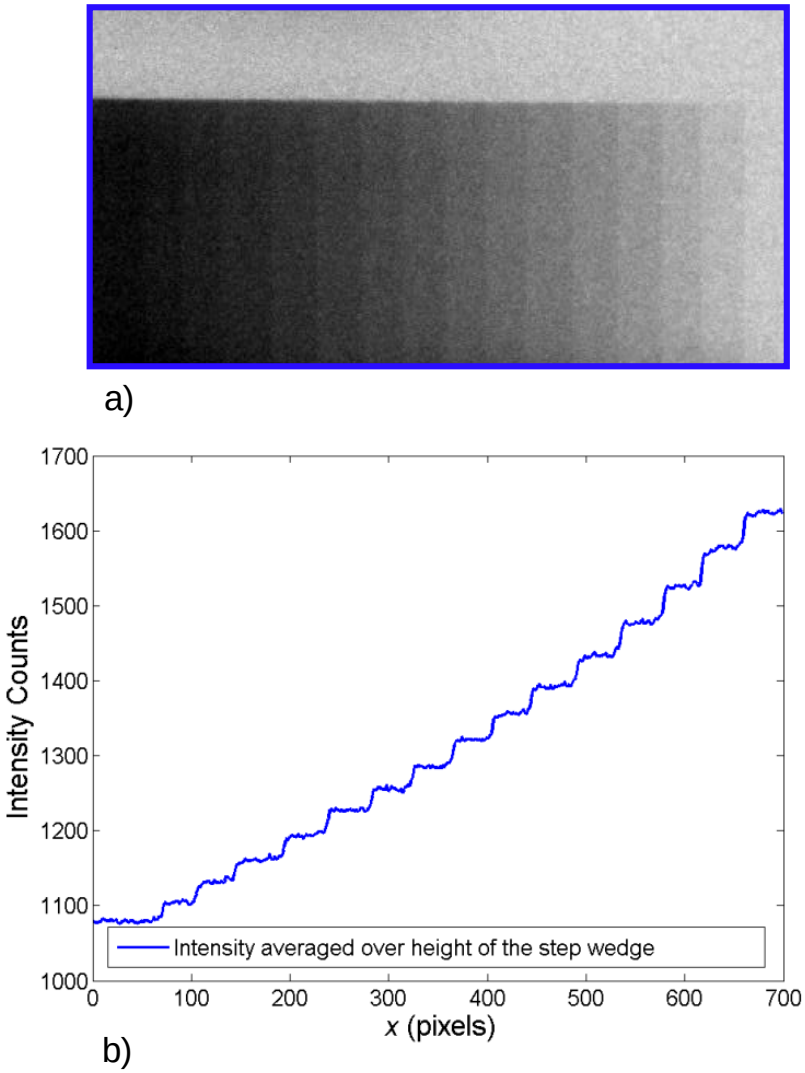

Fig. 38: Glass step-wedge: a) image, and b) intensity averaged over the height of the step wedge.

shown in Fig. 38a. At the left of the image, the x-rays have passed through 15 glass slides. From left to right, for about every 40 pixels, the thickness decreases by 0.96 mm resulting in the sixteen different intensity levels. Note that the right of the image corresponds to an area without the step wedge where the x-rays were attenuated only by the 20 mm of aluminum windows. This area defines I_0. Note that all intensities used herein have been corrected as described in Section 5.2 above.

The intensity in the image of Fig. 38a was averaged over the 25.4 mm height of the wedge resulting in the stepped plot of Fig. 38b. The intensity of each step was then averaged over its length in x of about 40 pixels producing the measured attenuation curve of Fig. 39. Then by least squares regression, the measured data were fit to Eq. (8) to solve for the mass x-ray attenuation coefficient resulting in A = 0.124 cm^2/g. Owing to brems radiation, the peak intensity of the flash x-rays should occur at about 150 keV. According to Ref. [40], at a photon energy of 150 keV, the attenuation coefficient through Pyrex glass is 0.139 cm^2/g, which is within a reasonable 12% of the current measurement.

The particle volume fraction of particle field is calculated with Eq. (10) and the use of two assumptions: 1) The soda lime spheres result in the same x-ray attenuation as the glass step-wedge, and 2) The thickness of particle field remains constant with w_0 = 68.6 mm. To test the former assumption, a calibration with a step-wedge consisting of soda lime spheres will be used in future calibrations.

Since only one flash x-ray image can be acquired per interaction experiment, images from different interactions are pieced together to form a pseudo-sequence. This method is justified by the

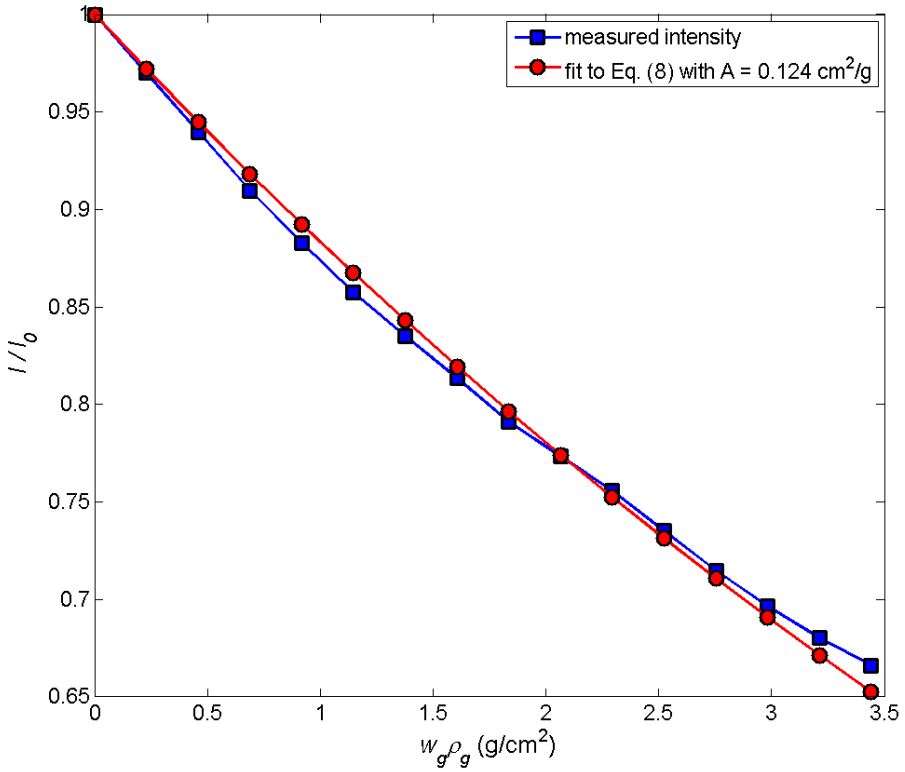

Fig. 39: Step-wedge intensity measurements and least-squares regression fit to Eq. (8) with A = 0.124 cm^2/g.

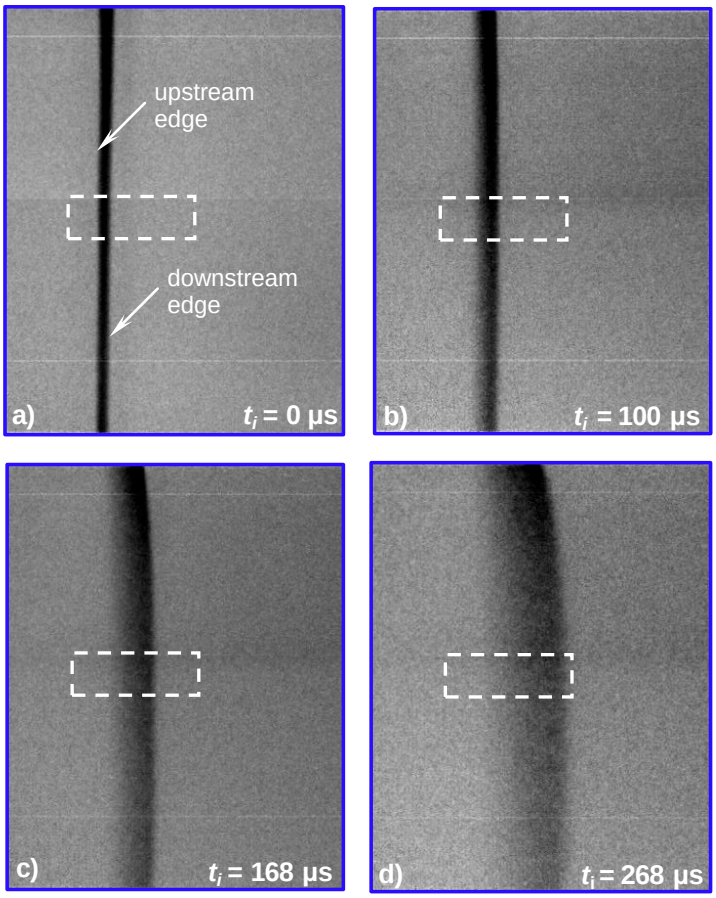

Fig. 40: Flash x-ray images showing the evolution of the particle field during M_s = 1.66 interactions at times: a) t_i = 0 µs, b) t_i = 100 µs, c) t_i = 168 µs, and d) t_i = 268 µs. The white rectangle shows the location used to produce the volume fraction profiles given in Fig. 41.

fact that fast-response pressure measurements and high-speed schlieren imaging have shown the interaction to be repeatable. A pseudo-sequence of images acquired during three different M_s = 1.66 interactions is presented in Fig. 40. The image fields-of-view are 50 × 64 mm^2 and their location in the test section is given in Fig. 37. The image in Fig. 40a corresponds to an undisturbed particle curtain prior to the arrival of the incident shock. From the image, an average streamwise intensity profile was produced is a similar fashion to that described in the imaging processing section above. The rectangle annotation in Fig. 40a shows the location for the profile. The volume fraction profile of the undisturbed curtain, which was calculated using the streamwise intensity profile and Eq. (10) is shown in Fig. 41 (t_i = 0 µs). At the wall-normal center of the test section, the peak volume fraction is about 21%, which is in good agreement with previous measurements that used imaging of the curtain and a precision scale. It is expected that the true volume fraction distribution is closer to a top-hat profile than the profile in Fig. 41 suggests. Two factors contribute to the apparent broadening of the displayed profile. The first is geometric blur, which is expected to broaden the apparent curtain width by a total of about 0.2 mm. The second contributor (as is illustrated in Fig. 36) is the angle θ between the source centerline and the streamwise location of the curtain of about 1.5-degrees. Although there

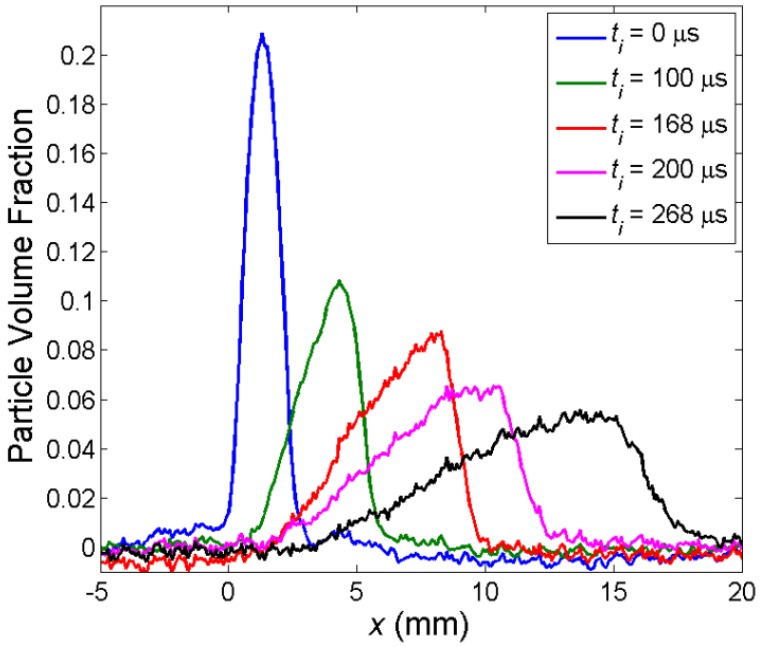

Fig. 41: Volume fraction profiles at five different interaction times based on averaged streamwise profiles in the area denoted in Fig. 40 and Eq. (10).

are bias errors in the measurements, the method shows promise and such errors can be reduced by translating the x-ray source to minimize θ.

As is shown in Fig. 40, following the arrival of the incident shock at the curtain and with continuing time, the particle field propagates downstream while spreading. Although previous schlieren imaging was able to capture such observations, it was not able to quantify the volume fraction of the field during an interaction. Conversely, the current measurements yield volume fraction profiles at four different interaction times, displayed in Fig. 41. The profiles were calculated using the pseudo-sequence of Fig. 40 and Eq. (10). The distribution of the streamwise volume fraction can be seen as it evolves with interaction time, providing unprecedented details of the particle field that otherwise would be hidden within its opacity. From t_i = 0-268 μs, the width of the particle field grows as it moves downstream and the peak volume fraction decreases from about 21% to about 5%. The field spreads in an asymmetric fashion having a steeper gradient in volume fraction on the downstream side of the field. Developing the capability to measure the particle volume fraction during an interaction accomplishes the first goal for the flash x-ray diagnostics. Having such diagnostics at hand augments further the unique capabilities of the MST to provide high-fidelity data for shock wave interactions with dense particle fields. These measurements represent a major achievement for the current project and quantitatively reveal particle dynamics of the spreading particle field that would not be discernable by any conventional measurement technique.

5.4. X-Ray Particle Velocimetry

The current work also evaluates the feasibility for making x-ray particle image velocimetry (PIV) measurements during a shock tube test. Such velocity data are necessary to directly evaluate the drag of the particles within the particle field, and its variation throughout the field. For this evalation, both flash x-ray channels were utilized as is shown in Fig. 42. Note that the schematic is in the end-view (*y*-*z*) plane. Owing to the detector readout time, velocimetry measurements during a shock tube test

require a double-exposure of the x-ray sources. The total angle between the sources θ_2 was about 10 degrees in order to illuminate the same portion of the test section. In future tests with a particle curtain, tracer particles will be mixed with the glass beads that form the curtain. In order to obtain tracer contrast, they must attenuate more than the surrounding glass beads. A good candidate for such a tracer is tin.

The current work used a test target consisting of 300-micron tin spheres adhered to a 5 mm thick acrylic sheet. As shown in Fig. 42, the target was aligned parallel to the streamwise dimension and placed near the spanwise center of the test section ($z = 0$). The source to object (target) distance along the spanwise coordinate Δz_{SO} was about 100 cm. The image (detector) to object distance along the spanwise coordinate Δz_{IO} was about 8.4 cm.

The field-of-view for the tracer imaging is given in Fig. 43. Since the sources were angled with respect to z-axis, the image from each source appeared on the detector at a different y-location. The lower rectangle represents the location of the image from the upper x-ray source (A) on the detector and the upper rectangle denotes the image from the lower source (B). The area where the rectangles overlap corresponds to the portion of the target that was exposed to both sources. The angle of the sources also resulted in the top portion of image A and the bottom portion of image B being blocked by the test section. From geometry, a stationary double-exposed object will appear in the image plane at two different y-locations at a spacing of:

$$\Delta y' = 2\Delta z_{IO} \tan\frac{\theta_2}{2} \tag{11}$$

Equation (11) and the experimental dimensions predict that a stationary, double-exposed object should appear with a spacing of about 14.7 mm, corresponding to 147 pixels.

To test the potential for applying particle velocimetry techniques to make measurements within the optically opaque particle curtain, the target with randomly distributed 300-micron tin spheres was imaged. Sample images of the 300-micron tin spheres that can serve as tracer particles are shown in

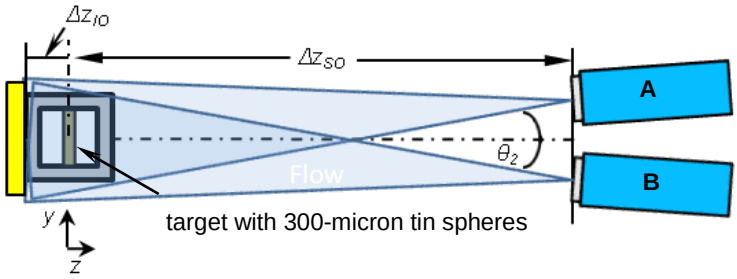

Fig. 42: Schematic of the dual-source configuration used for x-ray velocimetry measurements of a streamwise parallel particle field.

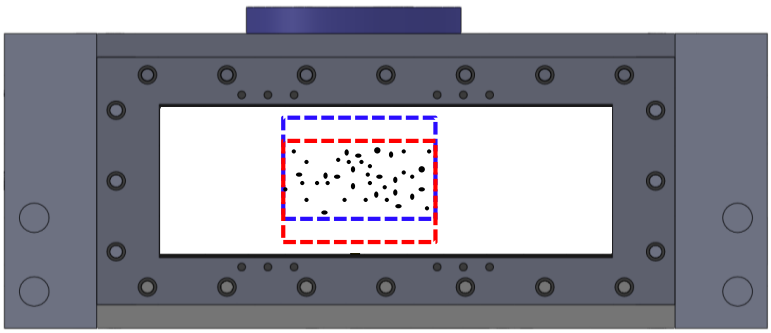

Fig. 43: Field-of-view for the x-ray particle imaging velocimetry evaluation.

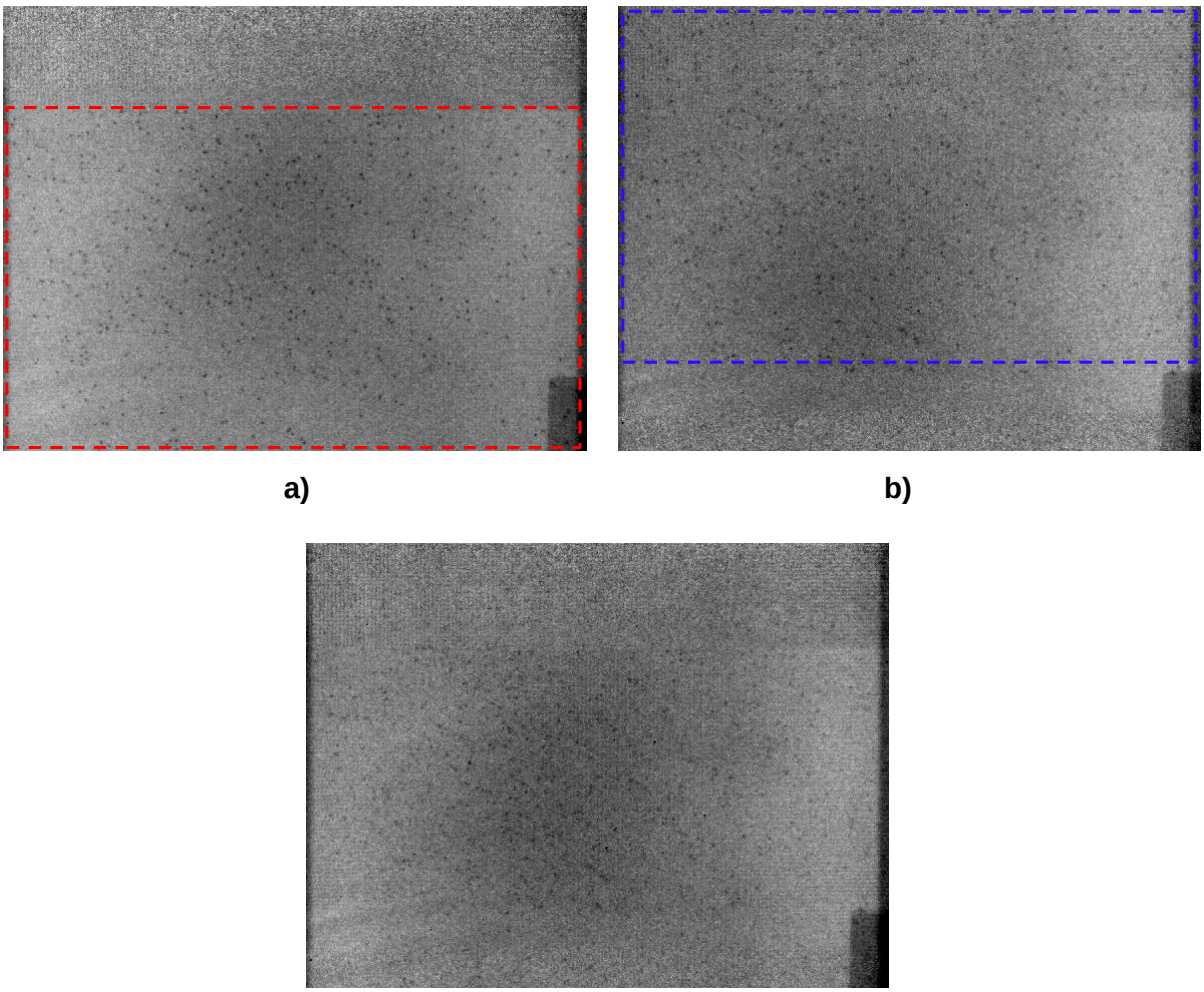

Fig. 44: Flash x-ray images of the target containing 300-micron tin spheres: a) image from tube head A, b) image from tube head B, and c) addition of Fig. 44a and Fig. 44b.

Fig. 44. All images have had the contrast adjusted to best show the tin spheres, which are observed as the dark spots in the images. At the time of these experiments, only one x-ray tube was available. Therefore, to test particle velocimetry applicability, the one tube was placed in tube head A (Fig. 42) and an image was acquired that is shown in Fig. 44a. The same tube was then placed in tube head B and another image of the stationary target was recorded that is shown in Fig. 44b. The useful areas of both images are shown with the rectangular annotations that are consistent with those in Fig. 43. As was discussed above, the image from each source will appear shifted in the y-direction and the apparent spacing between images of a particle should be given according to Eq. (11). To use the current setup in a shock tube experiment, it would be necessary to acquire a double-exposed image on the detector. To replicate such a double-exposure, the image in Fig. 44a was superimposed onto the image of Fig. 44b, resulting in the image of Fig. 44c.

The images in Fig. 44a and Fig. 44b were used to compute vector fields using the cross-correlation algorithm in the software package LaVision Davis 7.2. An autocorrelation algorithm was applied to the image in Fig. 44c. Four passes (three adaptive passes) were used to calculate the final vector field. An initial window shift with a displacement of Δy = 150 pixels (15 mm) was applied to

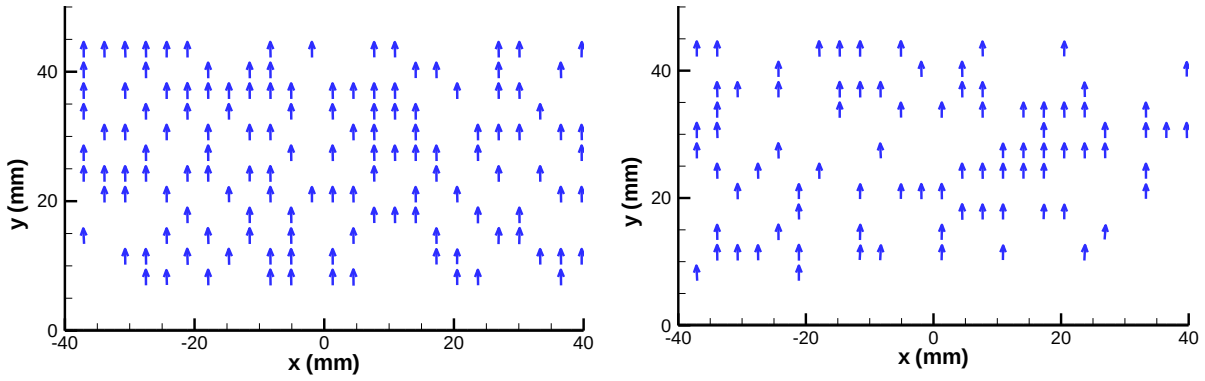

Fig. 45: X-ray PIV vector fields: a) cross-correlated field using the images of Fig. 44a and Fig. 45b, and b) vector field from the autocorrelation of Fig. 44c. The cross-correlated field has about 50% valid vectors compared to about 30% for the autocorrelation field.

the first pass to account for the geometrical shift. The first two passes had an interrogation window size of 64 × 64 pixels^2 (6.4 × 6.4 mm^2) and the final two passes used 32 × 32 pixels^2 (3.2 × 3.2 mm^2) windows. For the cross-correlated vector field, on each pass, a signal-to-noise filter removed vectors with a ratio of highest correlation peak to second highest correlation peak ratio Q_{12} less than 1.10. The vector field from the autocorrelation required a less stringent Q_{12} of 1.05 to return vectors. The velocity data were also filtered with a standard 3 × 3 median filter. In the median filter, the components of the velocity vector in question were compared to the median velocity components of the neighboring vectors. Vectors having a velocity component with a deviation outside the range of ±2σ (where σ is the standard deviation) from the median were removed.

The vector field from the cross-correlation of Fig. 44a and Fig. 44b is shown in Fig. 44a. The amount of valid vectors is about 50%. For a standard PIV application, this percentage would be considered quite low. However, for the novel application of the current flash x-ray system to an optically opaque medium, this result is promising. The average x displacement Δx is about -1.7 pixels, with a standard deviation Δx_{rms} of about 1.2 pixels. The average y displacement is about 150 pixels, with a standard deviation Δy_{rms} of about 1.2 pixels. The measured Δy is close to that approximated by experimental geometry and Eq. (11) and the measured Δx is close to zero as it should be for the stationary target. The vector field from the autocorrelation of Fig. 44c is given in Fig. 45b. The amount of valid vectors is about 20% lower than its cross-correlation counterpart. The average Δy and Δx are about 148 and 0.5 pixels, respectively. However, owing to the noisier image, the standard deviations Δy_{rms} and Δx_{rms} are about three times greater than those for the cross-correlated vectors. Although there is certainly room for improvement, it seems plausible that the current setup would work to measure velocities in an optically opaque field during a shock tube test. Ideas for improvement and future work are discussed below.

Unfortunately, budgetary and time constraints did not allow for velocimetry measurements during a shock tube test involving a particle field. With the limited life of the x-ray tubes (six were used in this work) it was possible to obtain the particle volume fraction data during an interaction, but it was only possible to test the feasibility for x-ray velocimetry measurements. The tests were however promising in suggesting that x-ray PIV measurements can be made in an optically thin curtain. There is a limitation for the current PIV setup. As is shown in Fig. 42, and Eq. (11), the apparent Δy displacements are dependent on the spanwise location z. In tests with a spanwise parallel curtain that is optically thick, the tracer particles will exist at many z locations. The fact that the measurements are integrated throughout the entire test volume will therefore result in many apparent Δy

displacements. With each interrogation window having many Δy displacements, PIV algorithms will fail. Fortunately, there is a solution to this problem.

The geometry of the current experimental setup could be advantageous to particle tracking velocimetry (PTV) measurements. Since PTV tracks individual particles, a vector would be given for each particle. High-speed schlieren imaging at the edges of the particle field and the fact that the shock-induced flow is one-dimensional suggest that the particle flow is predominantly one-dimensional. If one assumes one-dimensional flow, then the apparent Δy from PTV measurements could be used to determine the z location of a particle. This would result in a volumetric measurement of velocity through the entire test section width.

The demonstration that it is possible to make velocimetry measurements within the optically opaque particle field is extremely promising. Such diagnostics can provide a direct measure of the momentum transfer between the gaseous and solid phases during the shock-induced dispersal of a dense particle field. This data would be invaluable to increasing our understanding and ability to accurately model a number of explosives problems. With a working x-ray particle velocimetry system, the MST is now well equipped to handle the many complex compressible multiphase flow problems that are vital to the national interest.

6. Conclusions

Currently, owing to a lack of data, there are significant deficiencies in the understanding of the dynamics that occur following the impingement of a shock on a dense particle field. To remedy this, a unique Multiphase Shock Tube has been developed to study the interaction of a planar shock wave with a gas-solid mixture of particles having a volume fraction between the dilute and granular limits. To create a dense, isotropic particle field, a gravity-fed contoured seeding method was developed. The shock tube produced a planar shock that was driven into a curtain of 100-micron glass spheres, which had a volume fraction of about 19%.

Data from the novel facility were presented at incident shock Mach numbers of 1.66, 1.92, and 2.02 using high-speed schlieren imaging and fast-response pressure measurement systems. Following impingement of the incident shock on the curtain, transmitted and reflected shocks were observed that resulted in a particle drag that initially varied across the streamwise dimension of the curtain. Prominent expansion waves propagated downstream just after the transmitted shock, which were immediately followed by compression waves. Tens of microseconds after the onset of the interaction, the downstream edge of the particle curtain began to propagate noticeably. Eventually the upstream edge also began to show downstream motion, but at a slower velocity resulting in spread of the particle curtain. Pressure measurements and simple one-dimensional unsteady wave theory suggested that the difference in flow velocities across the curtain was initially of order 100 m/s. It is likely that the spread of the particle field is in part caused by the streamwise drag difference across the curtain.

Fast-response pressure measurements made 13 mm downstream of the curtain showed the unsteady pressures during an interaction with M_s = 1.66 to be about 35% greater than the baseline (without particles) case. In comparison, for M_s = 1.95, the peak pressures were about 46% greater than the baseline. The increase over the baseline occurred with the passage of the smooth compression waves and with the particle field crossing over the sensor locations. At about 64 mm downstream of the initial curtain location, the interaction pressure increases above the baseline were much smaller, which indicated that the pressure equilibrated across the curtain as it dispersed and propagated downstream. Pressure measurements were also made at about 0.43 m downstream of the interaction. The measurements provided a measure of momentum and energy flux losses associated with the interaction. For interactions at all three shock Mach numbers, the momentum and energy fluxes were 30-40% lower in the induced flow downstream of the transmitted shock compared to the baseline case.

Additional experiments have been conducted to obtain new drag coefficient data for spherical particles accelerated in shock-induced flows. The primary motivation for the experiments was to determine if compressibility as opposed to flow unsteadiness was the cause of the increased drag frequently reported to occur for shock-accelerated particles. High-speed schlieren imaging was used to observe the flow structure following the impingement of a planar shock on a 1 mm sphere. For all three Mach numbers, transient effects such as reflected bow shocks were observed. The imaging also revealed recompression shocks in the particle wakes for the two higher Mach numbers that were seen to interact with close enough particle spacing. The particle-particle interactions at the two higher Mach numbers increased the drag. Therefore, trajectories containing such interactions were not included in the reported drag measurements.

The particle drag coefficients were determined by fitting particle tracking velocimetry measurements to the drag relation. Data acquired over the induced flow Mach number range of about 0.7 to 1.0 clearly show that increasing the particle Mach number increases its drag coefficient by more than 50%. Furthermore, low values for the acceleration parameter indicate that flow unsteadiness is not expected to account for an increased sphere drag for this new data. Therefore it is concluded that the increased drag coefficients measured in the current work are caused by increased

compressibility and not flow unsteadiness, which additionally suggests a similar explanation for many previous shock tube experiments.

A flash x-ray measurement system has been developed to penetrate the optically opaque particle curtain. The novel use of the diagnostic provided a measure of the particle volume fraction and its evolution during a Mach 1.66 interaction. As the particle field spread and propagated downstream, the peak particle volume fraction decreased from about 21% to 5% over the span of about 300 μs. Furthermore, the streamwise gradient in the particle volume fraction was observed to be greater at the downstream side of the particle field. The flash x-ray system was also used to evaluate the feasibility of making x-ray particle image velocimetry (PIV) and particle tracking velocimetry (PTV) measurements. To make this assessment, a target containing 300-micron tin spheres was imaged with a single detector. The results were promising suggesting that x-ray PIV measurements can be made for interaction tests that involve an optically thin curtain. Furthermore, it was found that x-ray PTV may have the potential to provide volumetric particle velocity measurements.

The development of the Multiphase Shock Tube enables the study of shock interactions with dense particle fields, offering experimental capability to a previously inaccessible regime. Initial results discussed herein already are providing the data revealing the physics of such interactions. Future experiments will use these new capabilities to delve deeper into the behavior of shock-induced particle interactions, providing unprecedented data that can aid particle dynamics models of dense gas-solid flows.

7. Future Work

Since the accurate simulation of energetic material detonation is crucial to a variety of national interests involving explosive devices, many future experiments are planned utilizing the new capabilities developed under this program. To gain the physical understanding necessary for high-fidelity modeling requires moving from low-fidelity explosive field tests to scientifically controlled experiments. To accomplish this task our unique Multiphase Shock Tube (MST) will be utilized to provide a wide range of physical data concerning the particle dynamics of dense gas-solid flows. No such data presently exist, except those acquired under the current project as new capability was developed. New results would have an immediate impact upon the modeling and simulation of energetic materials. At the time this is written, no additional funding has been secured, in large part due to the constraints of the present fiscal environment, particularly for experimental efforts. However, the value of the new capability and the proposed follow-on work has been recognized by multiple funding programs within DOE and DoD, with an expressed desire to fund continuing work on this project. Once funds become available, several studies will be pursued, which will improve our fundamental understanding and our modeling abilities.

The novel use of flash x-ray diagnostics has provided the capability to delve even deeper into the physics of shock interactions with dense particle fields. With a working x-ray particle velocimetry system, the MST is now well equipped to handle many complex compressible multiphase flow problems that are vital to the national interest. Currently one of the greatest uncertainties in multiphase detonation modeling is the unsteady momentum transfer that occurs between the gaseous and solid phases. With the capability to make velocimetry measurements within the optically opaque field, this unknown will be addressed. The velocimetry data will be invaluable as it will provide direct measurements of particle drag, vastly increasing our understanding and ability to accurately model a number of explosives problems.

The presence of multiple particles in close proximity results in particle-particle interactions, which further complicate matters and constitute one of the key difficulties in predicting energy release. As was observed in the current work, particle shocks as well as wakes can interact and significantly alter a particle's trajectory and drag coefficient. Future work will focus on experimentally well-controlled methods to understand how particle spacing and compressibility influence particle-particle interactions. The ultimate goal will be to provide the physical building blocks that will develop understanding for dense particle fields.

Current MST diagnostics that involve high speed photography and particle tracking velocimetry (PTV) allow for velocity measurements of the particles, but not the surrounding gas. To gain physical insight and reduce measurement uncertainties in the particle drag coefficient, it is necessary to simultaneously measure the unsteady velocities of the surrounding fluid. To acquire this important complementary data, future efforts will also focus on the novel application of laser based methods that include laser Doppler velocimetry (LDV) and particle image velocimetry (PIV).

The one-of-a-kind MST with its novel sophisticated diagnostics allows for shock interactions with dense particle fields to be thoroughly studied. The ultimate outcome will be a greatly improved knowledge of shock-induced particle dispersal. Future studies focused on the underlying physics will help us to better address many problems vital to the national interest including vulnerability of weapons and structures to nearby explosions, blast mitigation, IED protection, and enhanced blasts.

8. Acknowledgements

The authors would like to thank Marcia Cooper, 2554, for her contributions to the conceptual design of the baseline shock tube. Wayne Trott and Jaime Castaneda, both now retired from 1512, made key contributions to the design and construction of the shock tube and particle curtain. The X-ray diagnostics were implemented with assistance from Kyle Thompson, Jerry Stoker, and Kevin Rolfe, all of 1522.

9. References

[1] Zhang, F., Frost, D. L., Thibault P. A., Murray, S. B. "Explosive Dispersal of Solid Particles," *Shock Waves*, Vol. 10, 2001, pp. 431-443.

[2] Rudinger, G., *Fundamentals of gas-particle flow*, Elsevier Scientific Publishing, New York, 1980.

[3] Igra, O., and Ben-Dor, G., "Dusty Shock Waves," *Applied Mechanics*, Vol. 41, 1988, pp. 379–437.

[4] Aizik, F., Ben-Dor, G., Elperin, T., Igra O., and Mond M. (1995) "Attenuation law of planar shock waves propagating through dust-gas suspensions", *AIAA Journal*, Vol. 33, 1995, pp. 953–955.

[5] Wang, B. Y., Wu1, Q. S., Wang, C., Igra O., and Falcovitz, J., "Shock wave diffraction by a square cavity filled with dusty gas," *Shock Waves*, Vol. 11, 2001, pp. 7-14.

[6] Rudinger, G., and Chang, A., "Analysis of nonsteady two-phase flow," *Physics of Fluids*, Vol. 7, 1964, pp. 658–663.

[7] Miura, H., and Glass, I.I., "On the passage of a shock wave through a dusty-gas layer," *Proceedings of the Royal Society A*, Vol. 385, 1985, pp. 85–105.

[8] Sheffield, S. A., Gustavsen, R. A., Alcon, R. R., Graham, R. A., and Anderson, R. U., "Particle Velocity and Stress Measurements in Low Density HMX," *High Pressure Science and Technology*, 1994, pp. 1377-1380.

[9] Anderson, R. U., Graham, R. A., and Holman, G. T., "Time-Resolved Shock Compression of Porous Rutile," *High Pressure Science and Technology*, 1994, pp. 1111-1114.

[10] Baer, M. R., and Nunziato, J. W., "A two-phase mixture theory for the deflagration-to-detonation transition (DDT) in reactive granular materials," *International Journal of Multiphase Flow*, Vol. 12, 1986, pp. 861-889.

[11] Baer, M. R., "Shock wave structure in heterogeneous reactive media," *Proceedings of the 21st International Symposium on Shock Waves*, 1997, pp. 923–927.

[12] Rogue, X.,Rodriguez, G., Haas, J. F., and Saurel, R., "Experimental and numerical investigation of the shock-induced fluidization of a particles bed," *Shock Waves*, Vol. 8, 1998, pp. 29-45.

[13] Seeger A, Affeld K, Goubergrits L, Kertzscher U, and Wellnhofer E (2001), "X-Ray-Based Assessment of the Three-Dimensional Velocity of the Liquid Phase in a Bubble Column," *Experiments in Fluids*, Vol. 31, pp. 193-201.

[14] Lee S J, and Kim G B (2003), "X-Ray Particle Image Velocimetry for Measuring Quantitative Flow Information Inside Opaque Objects," *Journal of Applied Physics*, Vol. 94, No. 5, pp.3620-3623.

[15] Xiao Y, Amano R S, Cai T, Li J, and He G (2003), "Particle Velocity on Solid-Propellant Surface Using X-Ray Real-Time Radiography," *AIAA Journal*, Vol. 41, No. 9, pp. 1763-1770.

[16] Anderson, J. A., *Modern compressible flow: with historical perspective*, McGraw-Hill, 2002.

[17] Glass, I. I., and Sislian, J. P., *Nonstationary Flows and Shock Waves*, Oxford Science Publications, 1994.

[18] McGlaun, J. M., Thompson, S. L., and Elrick, M. G., "A three-dimensional shock wave physics code," *International Journal of Impact Engineering*, Vol. 10, 1990, pp. 351-360.

[19] Sommerfeld, M., "The unsteadiness of shock waves propagating through gas-particle mixtures," *Experiments in Fluids*, Vol. 3, 1985, pp. 197–206.

[20] Igra, O., and Ben-Dor, G., "Dusty Shock Waves," *Applied Mechanics Reviews*, Vol. 41, No. 11, 1988, pp. 379-437.

[21] Igra, O., and Takayama, K., "Shock Tube Study of the Drag Coefficient of a Sphere in a Non-stationary Flow," *Proceedings of the Royal Society of London A*, Vol. 442, 1993, pp. 231-247.

[22] Hoerner, S. F., *Fluid-Dynamic* Drag, published by the author, Brick Town, NJ, 1965.

[23] Henderson, C. B., "Drag Coefficients of Spheres in Continuum and Rarefied Flows," *AIAA Journal*, Vol. 14, No. 6, 1976, pp. 707-708.

[24] Clift, R., Grace, J. R., and Weber, M. E., *Bubbles, Drops, and Particles*, Academic, New York, NY, 1978.

[25] Clift, R., and Gauvin, W. H., *Proceedings of CHEMECA '70*, Vol. 1, Butterworth, Melbourne, 1970, pp. 14-28.

[26] Loth, E., "Compressibility and Rarefaction Effects on Drag of a Spherical Particle," *AIAA Journal*, Vol. 46, No. 9, 2008, pp. 2219-2228.

[27] Parmar, M., Haselbacher, A., and Balachandar, S., "Improved Drag Correlation for Spheres and Application to Shock-Tube Experiments," *AIAA Journal*, Vol. 48, No. 6, 2010, pp. 1273-1276.

[28] Rodriguez, G., Grandeboeuf, P., Khelifi, M., and Haas, J. F., "Drag Coefficient Measurement of Spheres in a Vertical Shock Tube and Numerical Simulation," *Proceedings of the 19th International Symposium on Shock Waves*, Marseille, France, July 1993, pp. 43-48.

[29] Devals, C., Jourdan, G., Estivalezes, J. L., Meshkov, E. E., and Houas, L., "Shock Tube Spherical Particle Accelerating Study for Drag Coefficient Determination," *Shock Waves*, Vol. 12, 2003, pp. 325-331.

[30] Suzuki, T., Sakamura, Y., Igra, O., Adachi, T., Kobayashi, S., Kotani, A., and Funawatashi, Y., "Shock Tube Study of Particles' Motion Behind a Planar Shock Wave," *Measurement Science and Technology*, Vol. 16, 2005, pp. 2431-2436.

[31] Jourdan, G., Houas, L., Igra, O., Estivalezes, J. L., Devals, C., and Meshkov, E. E., "Drag Coefficient of a Sphere in a Non-Stationary Flow," *Proceedings of the Royal Society A*, Vol. 463, 2007, pp. 3323-3345.

[32] Tanno, H., Itoh, K., Saito, T., Abe, A., and Takayama, K., "Interaction of a Shock with a Sphere Suspended in a Vertical Shock Tube," *Shock Waves*, Vol. 13, No. 3, 2003, pp. 191-200.

[33] Sun, M., Saito, T., Takayama, K., and Tanno, H., "Unsteady Drag on a Sphere by Shock Wave Loading," Shock Waves, Vol. 14, No. 1-2, 2004, pp. 3-9.

[34] Skews, B. W., Bredin, M. S., and Efune, M., "Drag Measurement in Unsteady Compressible Flow; Part 2: Shock Wave Loading of Spheres and Cones," *R&D Journal of the South African Institute of Mechanical Engineering*, Vol. 23, No. 1, 2007, pp. 13-19.

[35] Crowe, C. T., Nicholls, J. A., and Morrison, R. B., "Drag Coefficients of Inert and Burning Particles Accelerating in Gas Streams," *Symposium (International) on Combustion*, Vol. 9, No. 1, 1963, pp. 395-406.

[36] Selberg, B. P., and Nicholls, J. A., "Drag Coefficient of Small Spherical Particles," *AIAA Journal*, Vol. 6, No. 3, 1968, pp. 401-408.

[37] Rudinger, G., "Effective Drag Coefficient for Gas-Particle Flow in Shock Tubes," *ASME Journal of Basic Engineering*, Vol. 92, 1970, pp. 165-172.

[38] Karanfilian, S. K., and Kotas, T. J., "Drag on a Sphere in Unsteady Motion in a Liquid at Rest," *Journal of Fluid Mechanics*, Vol. 87, Part 1, 1978, pp. 85-96.

[39] Selman, J, *The Fundamentals of Imaging Physics and Radiobiology*, Charles C Thomas Publisher, 2000.

[40] Hubnell, J. H., Seltzer, S. M., "Tables of X-Ray Mass Attenuation Coefficients and Mass Energy-Absorption Coefficients from 1 keV to 20 MeV for Elements Z = 1 to 92 and 48 Additional Substances of Dosimetric Interest," *NIST X-ray Attenuation Databases* [online database], URL: http://www.nist.gov/pml/data/xraycoef/index.cfm.

Distribution:

10 MS0619 Sandia Creative Group, 3654
1 MS0899 Technical Library, 9536 (electronic copy)